

Black hole-neutron star coalescence: Effects of the neutron star spin on jet launching and dynamical ejecta mass

Milton Ruiz,¹ Vasileios Paschalidis,² Antonios Tsokaros,¹ and Stuart L. Shapiro^{1,3}

¹*Department of Physics, University of Illinois at Urbana-Champaign, Urbana, IL 61801*

²*Departments of Astronomy and Physics, University of Arizona, Tucson, AZ 85719*

³*Department of Astronomy & NCSA, University of Illinois at Urbana-Champaign, Urbana, IL 61801*

Black hole-neutron star (BHNS) mergers are thought to be sources of gravitational waves (GWs) with coincident electromagnetic (EM) counterparts. To further probe whether these systems are viable progenitors of short gamma-ray bursts (sGRBs) and kilonovae, and how one may use (the lack of) EM counterparts associated with LIGO/Virgo candidate BHNS GW events to sharpen parameter estimation, we study the impact of neutron star spin in BHNS mergers. Using dynamical spacetime magnetohydrodynamic simulations of BHNSs initially on a quasicircular orbit, we survey configurations that differ in the BH spin ($a_{\text{BH}}/M_{\text{BH}} = 0$ and 0.75), the NS spin ($a_{\text{NS}}/M_{\text{NS}} = -0.17, 0, 0.23$ and 0.33), and the binary mass ratio ($q \equiv M_{\text{BH}} : M_{\text{NS}} = 3 : 1$ and $5 : 1$). The general trend we find is that increasing the NS prograde spin increases both the rest mass of the accretion disk onto the remnant black hole, and the rest mass of dynamically ejected matter. By a time $\Delta t \sim 3500 - 5500 M \sim 88 - 138 (M_{\text{NS}}/1.4 M_{\odot})$ ms after the peak gravitational wave amplitude, a magnetically-driven jet is launched only for $q = 3 : 1$ regardless of the initial NS spin. The lifetime of the jets [$\Delta t \sim 0.5 - 0.8 (M_{\text{NS}}/1.4 M_{\odot})$ s] and their outgoing Poynting luminosity [$L_{\text{Poynt}} \sim 10^{51.5 \pm 0.5}$ erg/s] are consistent with typical sGRBs luminosities and expectations from the Blandford-Znajek mechanism. By the time we terminate our simulations, we do not observe either an outflow or a large-scale magnetic field collimation for the other systems we considered. The mass range of dynamically ejected matter is $10^{-4.5} - 10^{-2} (M_{\text{NS}}/1.4 M_{\odot}) M_{\odot}$, which can power kilonovae with peak bolometric luminosities $L_{\text{kno}} \sim 10^{40} - 10^{41.4}$ erg/s with rise times $\lesssim 6.5$ h and potentially detectable by the LSST.

PACS numbers: 04.25.D-, 04.25.dg, 47.75.+f

I. INTRODUCTION

We are in a golden era of gravitational wave (GW) physics where the sensitivity of ground-based laser interferometers is rapidly increasing. During the first observing run *O1* [1], only 3 GW events from binary black hole (BBH) mergers were detected. The *O2* run observed the first GWs (GW170817) from the inspiral of a stellar compact binary [2], in which at least one of the companions was a neutron star. The progenitor of this event has been officially classified as a merging binary neutron star (BNS) system, although the possibility of a merging black hole-neutron star (BHNS) progenitor cannot be excluded (see e.g. [3, 4]). In addition, 7 new BBHs were detected [1]. Finally, during *O3*, whose sensitivity was increased by $\sim 50\%$ compared to *O1*, at least 53 GW event candidates have been reported [5].¹ These GW events can be classified as follows: a) 37 BBHs candidates; b) 7 BNS candidates. It should be noted that the progenitor of GW190425 is a BNS system with a total mass of $3.4_{-0.1}^{+0.3} M_{\odot}$, which is significantly different from the known population of Galactic BNS systems (see e.g. [7]); c) 4 events in the so-called mass gap (compact objects with masses of $3 - 5 M_{\odot}$ —see e.g. [8–10]); and d) 5 BHNS candidates, of which only one event has been confirmed (GW190814) and whose inferred individual masses are $23_{-0.9}^{+1} M_{\odot}$ and $2.59_{-0.08}^{+0.08} M_{\odot}$ [11]. It is worth noting that, although this event is listed in [5, 6] as a BHNS candidate with $> 99\%$ probability, due to the lack of any EM counterpart or

tidal signature, the nature of the lighter companion is uncertain (see e.g. [12–15]). If indeed the lighter binary companion is a NS then this would be the heaviest NS yet observed [16]. If, on the other hand, the binary companion is a BH then it would be the lightest BH observed to date. Notice the mass of the lightest stellar-mass BH candidate observed in X-rays is $3.8_{-0.5}^{+0.5} M_{\odot}$ [17].

Intense EM counterpart-observing campaigns preceding/following GW detections have led to the following EM detections: a) a weak transient EM signal [18, 19] (event GW150914-GBM, observed only by Fermi) that lasted 1 s and appeared 0.4 s after the detection of GW150914, the first event consistent with the inspiral and merger of a BBH; b) a MeV-scale EM signal lasting for 32 ms and occurring 0.46 s before GW170104 (also consistent with a BBH [20]), as reported by the AGILE mission [21]); c) EM counterparts across the spectrum reported by several observatories (see e.g. [22–28]) following the detection of GW170817. Its association with the transient GRB170817A [23] and the kilonova AT 2017gfo/DLT17ck [29] provides the best direct observational evidence so far that at least some sGRBs are indeed powered by BNS mergers, or by the merger of a stellar compact binary where at least one of the companions is a NS (or a hybrid star [30, 31]). The BNS-sGRB connection was anticipated in [32–34], and numerically demonstrated by self-consistent simulations in full general relativistic magnetohydrodynamics (GRMHD) of merging BNSs [35–37] and BHNSs [38, 39]. GW170817 and its EM counterpart signals have been used to impose some constraints on the physical properties of a NS (see e.g. [2, 40–49]), such as the maximum mass of a spherical NS, as well as its tidal deformability, equation of

¹ Recently 26 of these events have been officially confirmed, along with 13 new GW events reported for the first time in [6].

state, and radius (see [50–55] for reviews); d) an EM flare observed by the Zwicky Transient Facility, consistent with an ejected BBH merger remnant in the accretion disk of an active galactic nucleus that may be associated with GW190521 [56]; and e) a weak EM transient (GRB190425 event) ~ 0.5 s after GW190814 as reported in [57].

Unlike the EM counterparts associated with GW170817, the other candidate EM counterparts were not confirmed by other observatories/satellites operating at the same time. The absence of observable EM counterparts from candidate BHNS mergers may question their role as progenitors of the central engines that power sGRBs. Yet, GRMHD simulations in [38, 39] showed that BHNS remnants of $q = 3 : 1$ mergers can potentially launch magnetically-driven jets. Now early population synthesis studies found that the distribution of mass ratios q in BHNSs depends on the metallicity, and peaks at $q = 7 : 1$ [58, 59], but more recent work finds that it is generally less than $10 : 1$, and peaks at $q \approx 5 : 1$ [11, 60]. As pointed out in [61, 62], the larger the mass ratio, the higher the BH spin required for the NS companion to be tidally disrupted before reaching the innermost stable circular orbit (ISCO). So far in BBHs reported by the LIGO/Virgo scientific collaboration, BHs have high mass and/or low spins (see e.g. Table VI in [6]). If this trend continues for LIGO/Virgo BHNSs, then it is expected that LIGO/Virgo BHNS remnants would have negligible accretion disks and ejecta [63], which might disfavor their role as progenitors of sGRBs and kilonovae. However, the NS spin could have a strong impact on the tidal disruption and dynamical ejection of matter, affecting both sGRB and potential kilonovae signatures. It should be noted that the spins of the binary companions are only weakly constrained by current GW observations.

In this paper, we survey fully relativistic BHNS configurations on a quasicircular orbit undergoing merger in which the BH and/or the NS companions are spinning. We address two questions: a) *Can a moderate high-mass ratio BHNS binary be the progenitor of an engine that powers sGRBs?*; b) *Can the spin of a NS companion change the fraction of the dynamical ejection of matter that may drive potentially detectable kilonovae signatures?*

We consider BHNS configurations with mass ratios $q = 3 : 1$ and $q = 5 : 1$. In the first case the BH spin is $a_{\text{BH}}/M_{\text{BH}} = 0.75$, while in the latter one the BH is nonspinning. The NS spin has a spin $a_{\text{NS}}/M_{\text{NS}} = -0.17, 0, 0.23$ or 0.33 . In all cases, the star is threaded by a dynamically weak poloidal magnetic field that extends from the stellar interior into the exterior (as in a pulsar), and whose dipole magnetic moment is aligned with the orbital angular momentum of the binary. For purposes of comparison with our earlier studies [38, 39], the NS is modeled by a polytropic equation of state (EOS) with $\Gamma = 2$.

We find that the late inspiral and merger phases of the above BHNS binaries are roughly the same as in [64, 65], where the magnetic field is confined to the interior of the star. The fraction of the total rest-mass NS outside the horizon varies from $\lesssim 1\%$ to $\sim 15\%$ depending strongly on the binary mass ratio. The general trend is that *increasing the NS prograde spin increases both the mass of the accretion disk remnant*

and the unbound material (ejecta). In addition, NS spin leads to GW dephasing, with higher prograde spin increasing the number of GW cycles.

Consistent with our previous results in [39], we find that by $\Delta t \sim 3500 - 5500 M \approx 88 - 138 (M_{\text{NS}}/1.4 M_{\odot})$ ms following the GW peak emission a magnetically-driven jet emerges from the BH + disk remnant of BHNSs with mass ratio $q = 3 : 1$ regardless of the initial NS spin. However, the jet launching time depends strongly on the latter. As the initial NS prograde spin increases, the effective ISCO decreases and the separation at which the star is tidally disrupted increases. These two effects induce long tidal tails of matter that result in more baryon-loaded environments. Thus, stronger magnetic fields are required to overcome the baryon ram-pressure, delaying the launch of the jet while the fields amplify. Notice that jet launching may not be possible for all EOSs if the matter fall-back timescale is longer than the disk accretion timescale [66]. The lifetime of the jet [$\Delta t \sim 0.5 - 0.8 (M_{\text{NS}}/1.4 M_{\odot})$ s] and outgoing Poynting luminosity [$L_{\text{Poynt}} \sim 10^{51.5 \pm 0.5}$ erg/s] are consistent with typical sGRB (see e.g. [67–70]), and with the Blandford–Znajek (BZ) [71] luminosities [72]. These results are also consistent with a simple, “universal” model for BH + disk remnants proposed in [73].

The characteristic temperature of the disk remnant is $T \sim 10^{11}$ K (or ~ 8.6 MeV) and hence it may also emit a copious amount of neutrinos with peak-luminosity of 10^{53} erg/s [74, 75]. However, as the lifetime of this process might be too small to explain typical sGRBs [75], it has been suggested that BH + disk remnants powering sGRBs may be dominated initially by thermal pair production followed by the BZ process [76].

Finally, we find the dynamical ejection of matter is strongly affected by the initial NS spin. It ranges between $10^{-4.5}$ and $10^{-2} (M_{\text{NS}}/1.4 M_{\odot}) M_{\odot}$, and may induce kilonovae signatures with peak bolometric luminosities of $L_{\text{knova}} \sim 10^{40} - 10^{41.4}$ erg/s and rise times $\lesssim 6.5$ h, potentially detectable by the Large Synoptic Survey Telescope (LSST) survey [77] out to $O(200)$ Mpc. Similar conclusions were reached in eccentric BHNS mergers with spinning NSs in [78]. These preliminary results suggest that moderate high mass ratio BHNSs that undergo merger, where the NS companion has a non-negligible spin, may give rise to detectable kilonovae signatures even if magnetically-driven jets are absent.

The remaining sections of the paper are organized as follows: A short summary of our numerical methods and their implementation, along with our initial data and the grid structure used to solve the GRMHD equations, are presented in Sec. II. We present our results in Sec. III and conclusions in Sec. IV. Geometrized units ($G = c = 1$) are adopted throughout the paper except where stated explicitly.

II. NUMERICAL SCHEMES

The numerical methods used to evolve the BHNS binaries are the same as in [39]. Therefore, in this section we briefly introduce our notation and summarize our numerical schemes,

TABLE I. Initial properties of the evolved BHNS configurations. We list the mass ratio $q \equiv M_{\text{BH}} : M_{\text{NS}}$, where M_{BH} is the BH mass at infinite separation and M_{NS} the NS rest-mass (see [79] for details), the BH spin $a_{\text{BH}}/M_{\text{BH}}$, the NS spin $a_{\text{NS}}/M_{\text{NS}}$, which is either aligned or antialigned (indicated with a $-$ sign) with respect to the total angular momentum of the system. $T/|W|$ and P are the kinetic-to-binding-energy ratio and the rotation period in units of $(M_{\text{NS}}/1.4M_{\odot})$ ms of the NS, respectively. The dimensionless ADM mass $\bar{M} \equiv \kappa^{-1/2} M$ (here κ is the polytropic gas constant), the ADM angular momentum J of the system, and the orbital angular velocity Ω_0 . The label for each configuration includes successively: a mass ratio tag ($q = 3$ or $q = 5$), and a tag identifying the spin direction (m = antialigned or p = aligned) and its magnitude. In all configurations, the NS companions have a nondimensional rest-mass $\bar{M}_{\text{NS}} = 0.15$, and the initial $M \Omega_0$ corresponds to an orbital separation of about $D_0 \simeq 8.7M \sim 66(M_{\text{NS}}/1.4M_{\odot})$ km.

Model	q	$a_{\text{BH}}/M_{\text{BH}}$	$a_{\text{NS}}/M_{\text{NS}}$	$T/ W $	P (ms)*	\bar{M}^\dagger	J/M^2	$M \Omega_0$
q3NS0.0 [‡]	3:1	0.75	0.0	0.0	0.0	0.55	1.09	0.0328
q3NSm0.17	3:1	0.75	-0.17	0.009	3.2	0.55	1.09	0.0328
q3NSp0.23	3:1	0.75	0.23	0.016	2.4	0.55	1.09	0.0328
q5NS0.0 [‡]	5:1	0.0	0.0	0.0	0.0	0.83	0.52	0.0333
q5NSm0.17	5:1	0.0	-0.17	0.009	3.2	0.83	0.52	0.0333
q5NSp0.23	5:1	0.0	0.23	0.016	2.4	0.83	0.52	0.0333
q5NSp0.33	5:1	0.0	0.33	0.15	1.9	0.83	0.52	0.0333

*Normalized to $(M_{\text{NS}}/1.4M_{\odot})$. Note that the fastest known pulsar has a period of 1.40 ms [80].

[†] $\bar{M} \simeq 5.1M_{\odot}(M_{\text{NS}}/1.4M_{\odot})$.

[‡] Cases treated previously in [39].

along with the initial data. We refer the reader to [39] for further details.

Formulation and numerical scheme: We solve Einstein's equations for the gravitational field coupled to the MHD equations for the matter and magnetic field using the adaptive-mesh-refinement (AMR) Illinois GRMHD code embedded in the Cactus/Carpet infrastructure [81, 82]. This code uses the Baumgarte-Shapiro-Shibata-Nakamura (BSSN) formulation [83, 84] to evolve the metric, and employs moving puncture gauge conditions cast in first order form [85]. Additionally, the code solves the MHD equations in a conservative formulation [see Eqs.(27)-(29) in [86]] using high-resolution shock-capturing methods [87]. We set the damping parameter η appearing in the shift condition to $\eta = 3.3/M$ for BHNSs with mass ratio $q = 3 : 1$, and to $\eta = 1.2/M$ for those with mass ratio $q = 5 : 1$ (see Table I). Here M is the Arnowitt-Deser-Misner (ADM) mass of the system. Following [88, 89], we use the generalized Lorenz gauge to avoid the spurious magnetic fields between AMR levels due to numerical interpolations. We set the damping parameter $\xi \sim 5.5/M$ for configurations with mass ratio $q = 3 : 1$, and $\xi = 6.4/M$ for those with $q = 5 : 1$. Finally, we adopt a Γ -law EOS $P = (\Gamma - 1)\rho_0 \epsilon$ with $\Gamma = 2$, which allows shock heating during the evolution. Here P and ρ_0 are the pressure and the rest-mass density, respectively. As in standard hydrodynamic and MHD simulations, we integrate the ideal GRMHD equations everywhere, imposing a tenuous constant-density atmosphere $\rho_{0, \text{atm}} = 10^{-10} \rho_0^{\text{max}}(0)$, where $\rho_0^{\text{max}}(0)$ is the initial maximum value of the rest-mass

density of the NS.

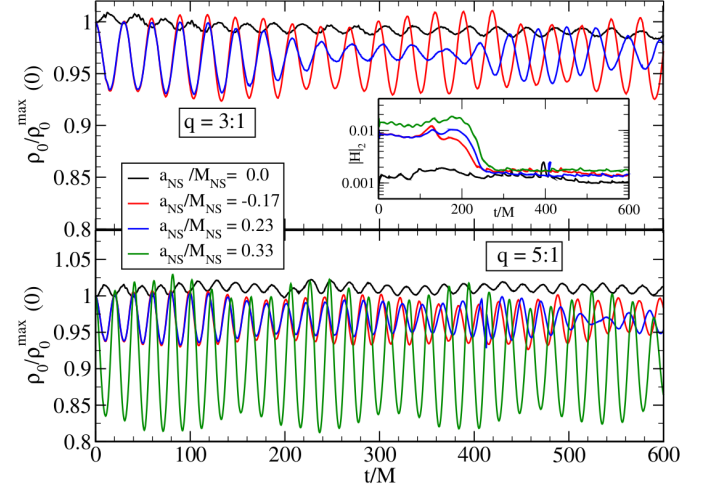


FIG. 1. Maximum value of the rest-mass density $\rho_0(t)$ normalized to its initial maximum value $\rho_0(0)$ during the early inspiral for the non-magnetized cases (see Table I). The inset shows the normalized L_2 norm of the Hamiltonian constraint (see Eqs. (40) and (41) in [64]) for the $q = 5 : 1$ cases. Due to the constraint damping used in our evolutions (see Eq. 19 in [90]), after about $t \sim 220M$ (or around one orbit), the Hamiltonian constraint falls roughly to the same low value for all cases in Table I regardless of the NS spin.

Initial data: The BHNS initial data used in this work have been presented in [91]. The configurations correspond to BHNS binaries on a quasicircular orbit undergoing merger with a separation chosen to be outside the tidal disruption radius [91]. We consider binaries with mass ratio $q = 3 : 1$, in which the BH companion has an initial spin parameter $a_{\text{BH}}/M_{\text{BH}} = 0.75$ (M_{BH} is the BH Christodoulou mass [92]) aligned with the total orbital angular momentum of the system, and binaries with mass ratio $q = 5 : 1$ with a non-spinning (irrotational) BH companion (see Table I). In all cases considered here, the companion has a compaction of $\mathcal{C} = \mathcal{M}_{\text{NS}}/R_{\text{NS}} = 0.145$, where \mathcal{M}_{NS} and R_{NS} are the ADM mass and the circumferential radius of the star in isolation. Note that for a polytropic EOS with $\Gamma = 2$, the maximum mass configuration has a compaction $\mathcal{C} = 0.215$. For comparative purposes, we rescale the rest-mass of the star as $M_{\text{NS}} = 1.4M_{\odot}(\kappa/\kappa_L)^{1/2}$, and hence the maximum rest-mass density of the star is $\rho_0^{\text{max}} = 8.92 \times 10^{14} (1.4M_{\odot}/M_{\text{NS}})^2 \text{ g/cm}^3$. Here, κ is the polytropic gas constant used to compute the initial data and defined as $\kappa = P/\rho_0^2$, and $\kappa_L = 189.96 \text{ km}^2$.

Following [93], to induce spin we endow an irrotational NS with an uniform angular velocity by modifying the fluid velocity as $v^i = v_{\text{irrot}}^i + \epsilon^i_{jk} \Omega^j x^k$, where $v^i = u^i/u^0$ is the coordinate velocity of the fluid, u^μ is the fluid 4-velocity, Ω^j is an angular velocity of the NS, and ϵ^i_{jk} is the Levi-Civita symbol. As shown in Table I, we endow the NS with spins ranging between -0.17 and 0.23 for the two BHNS mass ratios considered here. In addition, to further assess if highly spinning NS companions can induce potentially observable EM counterparts in BHNSs with moderate mass ratios, we consider a

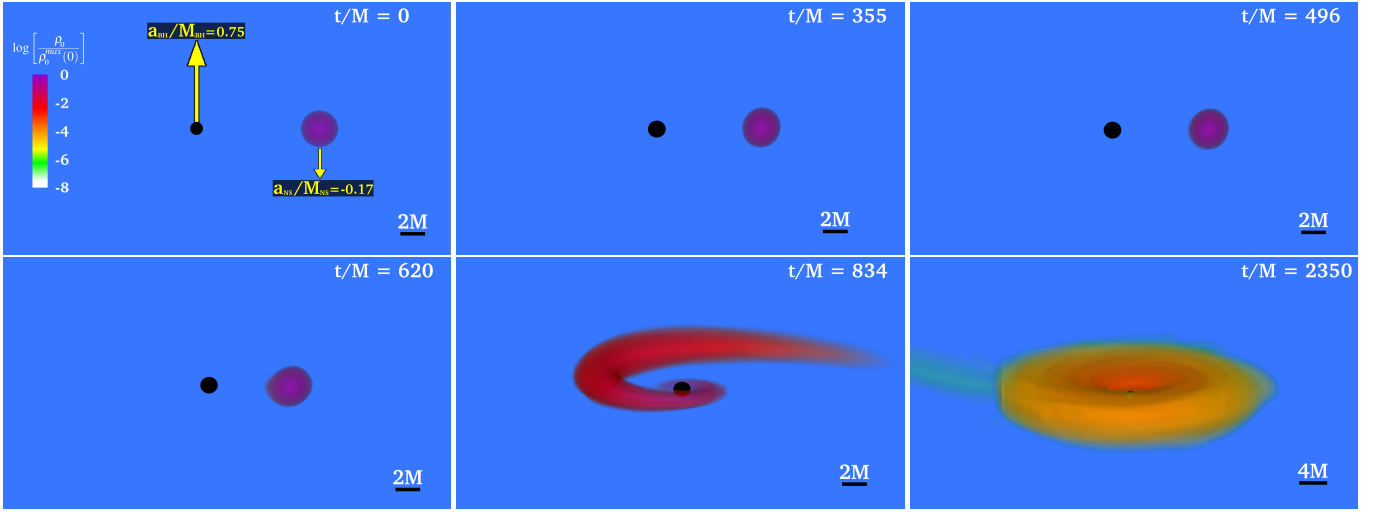


FIG. 2. Volume rendering of rest-mass density ρ_0 , normalized to its initial NS maximum value $\rho_0 = 8.92 \times 10^{14} (1.4M_\odot/M_{\text{NS}})^2 \text{g/cm}^3$ (log scale) at selected times for the nonmagnetized case q3NSm0.17 (see Table I). The BH apparent horizon is shown as a black sphere. Top panels focus on the binary inspiral, while bottom ones focus on the NS tidal disruption and disk formation. Despite the central density oscillations, the shape of the NS is practically unaffected by spin, and remains nearly spherical during the first five of the seven orbits prior to merger. Here $M = 2.5 \times 10^{-2} (M_{\text{NS}}/1.4M_\odot) \text{ms} = 7.58 (M_{\text{NS}}/1.4M_\odot) \text{km}$.

more extreme case ($a_{\text{NS}}/M_{\text{NS}} = 0.33$) for $q = 5 : 1$. In order to measure the spin of the NS, we compute its quasilo-cal angular momentum J_{ql} [94, 95], and normalize it to the rest-mass $J_{\text{ql}}/M_{\text{NS}}^2 = a_{\text{NS}}/M_{\text{NS}}$. If instead we normalized by its ADM mass (in isolation) the dimensionless spin values will increase correspondingly (e.g. our more extreme case with spin $a_{\text{NS}}/M_{\text{NS}} \sim 0.33$ becomes ~ 0.35). Using the measured value of J_{ql} , and the rest-mass M_{NS} , we adopt the Cook code [96–98] to generate equilibrium rotating neutron star models in isolation with these values of angular momentum and rest-mass, and compute the ratio of kinetic-to-gravitational potential energy $T/|W|$ as well as the spin period P that we list in Table I. All our cases have an estimated $T/|W| < 0.25$, and hence the NS is stable against the dynamical bar mode instability [84, 99, 100]. While our case with spin $a_{\text{NS}}/M_{\text{NS}} = 0.33$ might be unstable to the secular $m = 2$ -bar mode instability [100, 101], we point out that the $T/|W|$ values we provide are only estimated values in isolation.

As the new fluid velocity field no longer satisfies the hydrostatic equations, the NS undergoes small radial oscillations. Fig. 1 shows the relative changes in the central rest-mass density during the early inspiral for all cases in Table I. In contrast to the quasiequilibrium (irrotational) case, where the amplitude of the oscillations stays below $\sim 1\%$, the amplitude of the oscillations in cases $a_{\text{NS}}/M_{\text{NS}} = -0.17$ and 0.23 (see Table I) is larger but remains below $\sim 8\%$, and below $\sim 16\%$ in our extreme case ($a_{\text{NS}}/M_{\text{NS}} = 0.33$). The inset shows the L_2 norm of the Hamiltonian constraint for cases with mass ratio $q = 5 : 1$ during the early inspiral. We observe that due to the constraint damping (see Eq. 19 in [90]) used in our numerical evolutions, the constraint violation induced by our *ad-hoc* prescription of the new fluid velocity is damped and propagated away after roughly one orbit (or $t \lesssim 220M$). Similar results

are observed on the other cases in Table I.

Next, we evolve the above configurations until about two orbits before tidal disruption. At that point, the NS is threaded by a dynamically weak, dipolar magnetic field induced by a vector potential generated by a current loop inside the star (see Eq. 2 in [103]). As in [38, 39], we choose the current I_0 and the radius of the loop r_0 such that the magnetic-to-gas-pressure ratio at the center of the NS is $P_{\text{mag}}/P_{\text{gas}} = 10^{-2.5}$ (see Fig. 2 in [36]). The resulting magnetic field at the pole of the star turns out to be $B_{\text{pole}} \sim 6 \times 10^{15} (1.4M_\odot/M_{\text{NS}}) \text{G}$. As pointed out in [38], although we choose an astrophysically large magnetic field, it is dynamically unimportant in the stellar interior and does not affect the late inspiral or the merger phases. We do expect that the outcome of our numerical results will apply to other dynamically weak field choices because the magnetic field amplification following merger will be mainly triggered by magnetic winding and the magneto-rotational-instability (MRI) [104].

On the other hand, to capture one of the properties of the force-free conditions that likely characterize the NS exterior (magnetic-pressure dominance), we set a variable and low-density magnetosphere outside the star such that the magnetic-to-gas pressure ratio is $\beta^{-1} = P_{\text{gas}}/P_{\text{mag}} = 0.01$ everywhere [38]. This one-time reset of the low-density magnetosphere increases the total rest-mass on the entire grid by less than 1%.

Grid structure: The grid hierarchies used to evolve the BHNS binaries with mass ratio $q = 3 : 1$ and $q = 5 : 1$ are the same as those used to evolve models Tilq3sp0.75 and Aliq5sp0.0 (see Table II of [39]), respectively. They consist of two sets of nested refinement levels centered on both the BH and the NS. In all cases, the NS is covered by eight refinement levels, while the BH companion is covered by nine refinement levels for $q = 3 : 1$ cases, or by eight levels for

TABLE II. Summary. Case's name starting with an NM (or an M) denotes a nonmagnetized (or magnetized) evolution. $a_{\text{BH}}/M_{\text{BH}}$ denotes the spin of the BH remnant, and ΔE_{GW} and ΔJ_{GW} are the fraction of energy and angular momentum carried away by GWs, respectively. The kick velocity due to recoil is denoted by v_{kick} in km/s, M_{disk} is the fraction of the rest-mass of the material outside the horizon near the end of the simulation, \dot{M} is the rest-mass accretion rate computed via Eq. (A11) in [102], and $\tau_{\text{disk}} \sim M_{\text{disk}}/\dot{M}$ its lifetime in units of $(M_{\text{NS}}/1.4M_{\odot})$ s, α_{SS} is the Shakura–Sunyaev viscosity parameter, and $B^2/(8\pi\rho_0)$ is the space-averaged value of the force-free parameter in a cubical region of length $2R_{\text{BH}}$ above the BH poles near the end of the simulation. Here R_{BH} is the radius of the BH horizon. B_{rms} is the rms value of the magnetic field above the BH poles in units of $(1.4M_{\odot}/M_{\text{NS}})$ G, L_{Poynt} is the Poynting luminosity driven by the jet in units of erg/s and time-averaged over the last $500M \sim 12.5(M_{\text{NS}}/1.4M_{\odot})$ ms of the evolution, v_{eje} and M_{eje} are the mass-averaged velocity and rest-mass of the unbound material, while L_{kno} and t_{peak} are the peak luminosity and the rise time of the potential kilonova in units of erg/s and days, respectively. A dash symbol denotes no corresponding/unavailable value.

Case	$a_{\text{BH}}/M_{\text{BH}}$	$\Delta E_{\text{GW}}/M$	$\Delta J_{\text{GW}}/J$	v_{kick}	$M_{\text{disk}}/M_{\text{NS}}$	$\dot{M}(M_{\odot}/\text{s})$	τ_{disk}	α_{SS}	$B^2/(8\pi\rho_0)$	B_{rms}	L_{Poynt}	v_{eje}	M_{eje}	L_{kno}	t_{peak}
NMq3NS0.0 [†]	0.89	0.97%	14.89%	54.20	10.90%	0.39	0.4	—	—	—	—	—	—	—	—
NMq3NSm0.17	0.89	1.14%	13.10%	44.62	10.84%	0.46	0.3	—	—	—	—	0.24	$10^{-2.4}$	$10^{41.2}$	0.18
NMq3NSp0.23	0.90	1.10%	14.48%	63.96	14.56%	0.28	0.7	—	—	—	—	0.29	$10^{-2.3}$	$10^{41.2}$	0.18
Mq3NS0.0 [†]	0.85	1.11%	14.91%	54.20	10.00%	0.25	0.5	0.01 – 0.03	$10^{2.0}$	$10^{15.2}$	$10^{51.2}$	—	—	—	—
Mq3NSm0.17	0.85	1.20%	12.90%	46.40	8.78%	0.29	0.5	0.01 – 0.03	$10^{2.0}$	$10^{15.1}$	$10^{51.6}$	0.25	$10^{-2.1}$	$10^{41.3}$	0.25
Mq3NSp0.23	0.87	1.12%	14.60%	64.81	14.17%	0.23	0.8	0.01 – 0.03	$10^{2.1}$	$10^{15.2}$	$10^{52.1}$	0.27	$10^{-2.0}$	$10^{41.4}$	0.27
NMq5NS0.0 [†]	0.42	1.07%	20.07%	67.96	0.29%	0.02	0.2	—	—	—	—	—	—	—	—
NMq5NSm0.17	0.42	1.00%	19.56%	34.74	0.28%	0.02	0.2	—	—	—	—	0.26	$10^{-4.7}$	$10^{40.0}$	0.01
NMq5NSp0.23	0.42	1.08%	20.29%	62.88	0.65%	0.12	0.1	—	—	—	—	0.27	$10^{-3.7}$	$10^{40.4}$	0.02
NMq5NSp0.33	0.43	1.07%	20.35%	91.10	1.23%	0.15	0.1	—	—	—	—	0.33	$10^{-3.5}$	$10^{40.6}$	0.04
Mq5NS0.0 [†]	0.42	1.05%	19.63%	69.96	0.53%	0.04	0.2	—	$10^{-3.0}$	$10^{12.3}$	—	—	—	—	—
Mq5NSm0.17	0.42	1.00%	19.43%	36.82	0.53%	0.02	0.3	—	$10^{-3.2}$	$10^{12.4}$	—	0.25	$10^{-4.7}$	$10^{40.0}$	0.01
Mq5NSp0.23	0.42	1.06%	20.14%	70.31	1.04%	0.10	0.1	—	$10^{-3.1}$	$10^{12.1}$	—	0.27	$10^{-3.7}$	$10^{40.4}$	0.03
Mq5NSp0.33	0.43	1.06%	20.20%	93.80	1.42%	0.12	0.2	—	$10^{-2.9}$	$10^{12.7}$	—	0.35	$10^{-3.5}$	$10^{40.6}$	0.04

[†] Cases treated previously in [39].

$q = 5 : 1$ cases. The finest resolution box has a half length of $\sim 1.5 R_{\text{BH}}$ around the BH and $\sim 1.2 R_{\text{NS}}$ around the NS. These choices resolve the initial equatorial radius of the BH apparent horizon by around 40 grid points, and the initial NS equatorial radius by around 42 grid points. In all cases we impose reflection symmetry across the orbital plane ($z = 0$).

III. RESULTS

The basic dynamics and outcomes of irrotational NS cases in Table II have been previously described in [38, 39, 105]. There it was found that, in contrast to the high mass ratio cases where the NS basically plunges into the BH, the NS in $q = 3 : 1$ cases is tidally disrupted before reaching the ISCO. This resulted in long tidal tails of matter that eventually settle down, forming a significant accretion disk around the BH regardless of the magnetic field content (see Figs. 2 and 3).

In the magnetized cases, matter wrapping around the BH drags the frozen-in magnetic field into a predominantly toroidal configuration. However, initially the magnetic field lines connect the star with the poles of the BH, and later the low-density debris ejected during the tidal disruption remains connected to the accretion disk via these field lines (see top panels in Figs. 3 and 4), as a result, the external magnetic field maintains a strong poloidal component. Magnetic winding and the MRI then amplify the magnetic field

above the BH poles from $\sim 10^{13}(1.4M_{\odot}/M_{\text{NS}})$ G to $\sim 10^{15}(1.4M_{\odot}/M_{\text{NS}})$ G, when the accretion disk settles down. This amplification induces high magnetic pressure gradients above the BH poles that, when the regions above the BH poles approach force-free values ($B^2/8\pi\rho_0 \gg 1$), lead to the launching of a mildly relativistic outflow with a Lorentz factor $\Gamma_L \gtrsim 1.2$ confined inside a tightly wound, helical magnetic field funnel—an incipient jet (see bottom panels in Figs. 3 and 4). Here B and ρ_0 are the strength of the magnetic field and the rest-mass density, respectively. The lifetime of the jet and its associated luminosity are consistent with typical sGRBs [67–70], as well as with the BZ mechanism [71, 73].

A. Mass ratio $q = 3 : 1$

Figure 2 shows snapshots of the rest-mass density at selected times for NMq3NSm0.17 (see Table II for an explanation of the augmented case labels). We observe that although the star undergoes small radial oscillations due to our *ad hoc* prescription for the NS spin (see Fig. 1), the shape of the star is nearly spherical during the first five of the almost seven inspiral orbits before the binary merger (see top panels in Fig. 2). Bottom panels focus on the NS tail deformation, merger, and the subsequent formation of a quasistationary disk, as matter having larger specific angular momentum wraps around the BH. Similar behavior is observed in the other cases independent of the magnetic field (see Table II). However, we observe

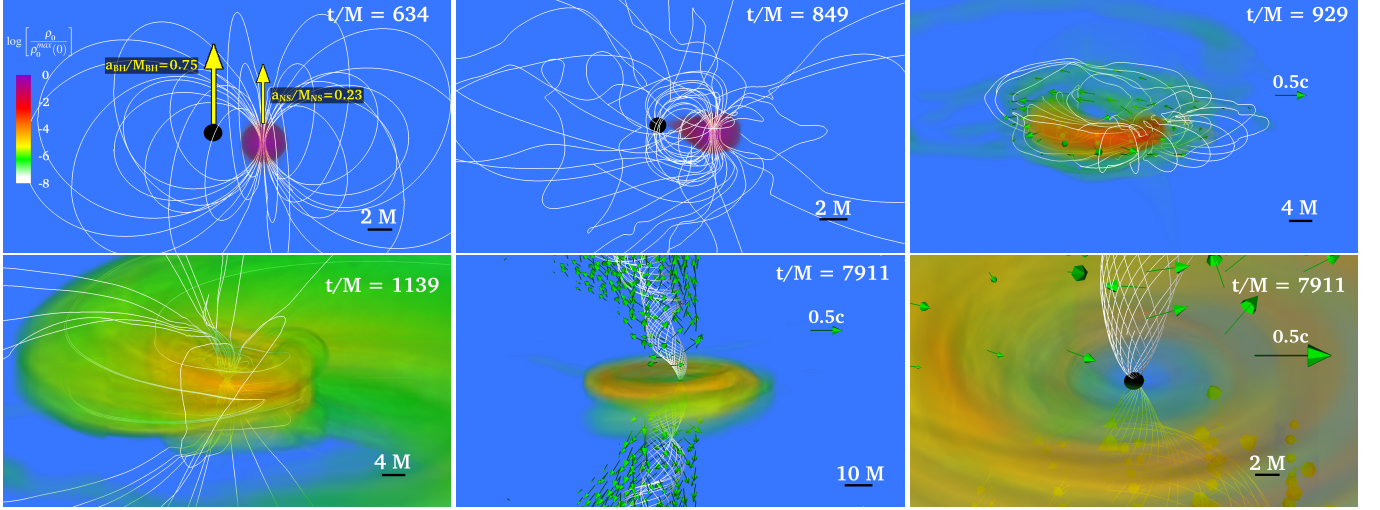


FIG. 3. Volume rendering of rest-mass density ρ_0 normalized to its initial NS maximum value $\rho_0 = 8.92 \times 10^{14} (1.4M_\odot/M_{\text{NS}})^2 \text{g/cm}^3$ (log scale) at selected times for Mq3NSp0.23 (see Table I). Bottom panels highlight the emergence of the magnetically-driven jet. White lines denote the magnetic field, arrows denote the fluid velocity, while the BH apparent horizon is shown as a black sphere. Here $M = 2.5 \times 10^{-2} (M_{\text{NS}}/1.4M_\odot) \text{ms} = 7.58 (M_{\text{NS}}/1.4M_\odot) \text{km}$.

that the larger the NS prograde spin is, the further out the NS disruption take place.

Notice that as the BH spin increases the ISCO decreases, and hence the tidal disruption effects become more pronounced, resulting in long tidal tails that eventually wrap around the BH forming the accretion disk. Similarly, as the prograde NS spin increases, the effective ISCO decreases (see e.g. [106]). Additionally, as the magnitude of the NS spin increases, the star becomes less bound, and the tidal separation radius r_{tid} (the separation at which tidal disruption of the NS begins) increases, resulting also in more pronounced disruption effects. This effect can be easily understood by estimating r_{tid} through a simple Newtonian argument. Equating the inward gravitational force exerted by the NS on its fluid elements with the BH's outgoing tidal force and the outgoing centrifugal force we find that (see also [78] for a similar expression)

$$r_{\text{tid}}/M_{\text{BH}} \simeq q^{-2/3} \mathcal{C}^{-1} [1 - \Omega^2 M_{\text{NS}}^2 \mathcal{C}^{-3}]^{-1/3}, \quad (1)$$

where $\Omega = a_{\text{NS}} M_{\text{NS}}/I$. Here I is the moment of inertia of the star. Therefore, the larger the magnitude of the NS spin, the larger r_{tid} , and hence the more material spreads out to form the disk. Consistent with the above predictions, we find that the accretion disk in our extreme cases has a rest mass ranging between $\sim 9\%$ (for Mq3NSm0.17) and $\sim 14.2\%$ (for Mq3NSp0.23) of the total rest-mass of the NS (see top panel in Fig. 5). Slightly more massive disks are found in the nonmagnetized cases (see Table II). In all cases, the BH remnant has a mass of $\simeq 4.76M_\odot (M_{\text{NS}}/1.4M_\odot)$, and its spin is $a_{\text{BH}}/M_{\text{BH}} \simeq 0.9$ for the nonmagnetized cases, and $a_{\text{BH}}/M_{\text{BH}} \simeq 0.85$ for the magnetized cases. These values seem to be unaffected by the initial NS spin. Similar behavior was reported in spinning BNS mergers [107].

By contrast to the nonmagnetized cases, where the BH + disk remnant settles down into an almost steady config-

uration after $\sim 800M \simeq 20(M_{\text{NS}}/1.4M_\odot) \text{ms}$ following merger (see bottom panels of Fig. 2), the magnetized cases launch a mildly relativistic outflow confined in a tightly wound, helical magnetic field funnel after $\sim 3500\text{--}5500M \simeq 88\text{--}138(M_{\text{NS}}/1.4M_\odot) \text{ms}$ (see below) following merger (see bottom panels in Figs. 3 and 4).

To probe if magnetic turbulence is operating within the accretion disk, we first verify that the wavelength of the fastest growing MRI mode λ_{MRI} in all our cases is resolved by $\gtrsim 5$ grid points (see Fig. 9 in [39]). It is likely that the MRI is at least partially captured in our simulations [108]. We also compute the Shakura–Sunyaev viscosity α_{SS} parameter through Eq. 26 in [109]. We find that in the innermost $12M \simeq 91(M_{\text{NS}}/1.4M_\odot) \text{km}$ of the disk and outside the ISCO, α_{SS} ranges between 0.01 and 0.03 (see Table II), consistent with values reported in earlier accretion disk studies [108, 110]. Therefore, it is expected that magnetic turbulence driven by MRI is operating to some degree in our simulations and drives the quasisteady accretion. However, farther studies at higher resolution are required to confirm these results. We compute the rest-mass accretion rate \dot{M} through Eq. A11 in [102] and found after $\sim 1500M \simeq 38(M_{\text{NS}}/1.4M_\odot) \text{ms}$ following the merger, the accretion begins to settle to a quasi-stationary state and decays slowly afterward. In magnetized cases, we find that \dot{M} is roughly $0.3M_\odot/\text{s}$ (see Table II) once the outflow reaches a height of $\sim 100M \simeq 760(M_{\text{NS}}/1.4M_\odot) \text{km}$. At that time, the disk has a mass of $\sim 0.13M_\odot (M_{\text{NS}}/1.4M_\odot)$ for Mq3NSm0.17 and Mq3NS0.0, and of $\sim 0.2M_\odot (M_{\text{NS}}/1.4M_\odot)$ for Mq3NSp0.23 (see Table II). Hence the disk (jet's fuel) is expected to be accreted in $\Delta t \sim M_{\text{disk}}/\dot{M} \sim 0.5\text{--}0.8(M_{\text{NS}}/1.4M_\odot) \text{s}$, consistent with the lifetime of typical sGRBs [111].

As pointed out in [38], following tidal disruption, magnetic winding and the MRI amplify the magnetic field and induce magnetic pressure gradients above the BH poles

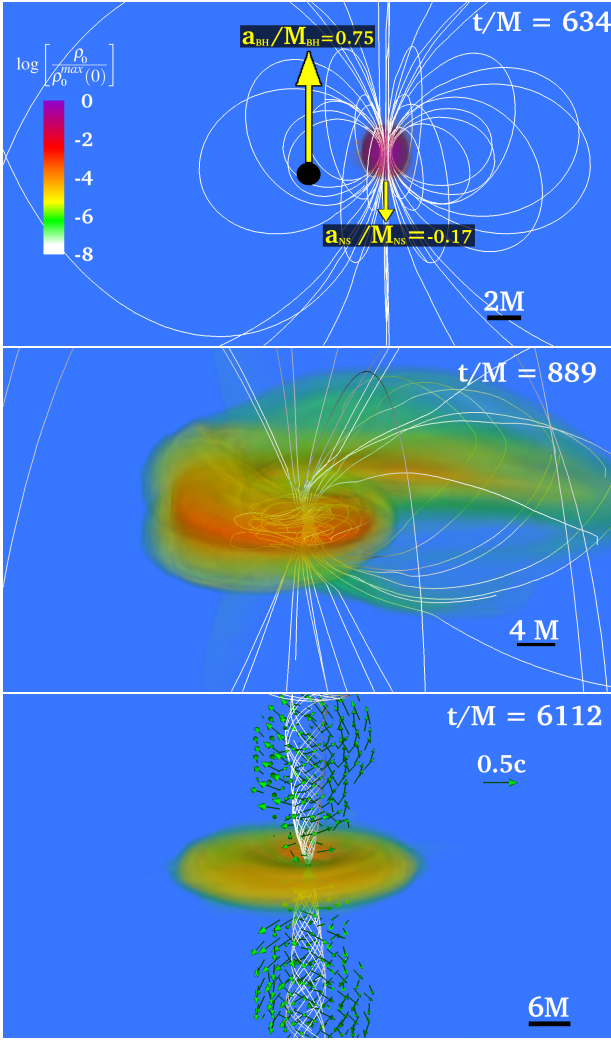


FIG. 4. Same as Fig. 3 but for Mq3NSm0.17.

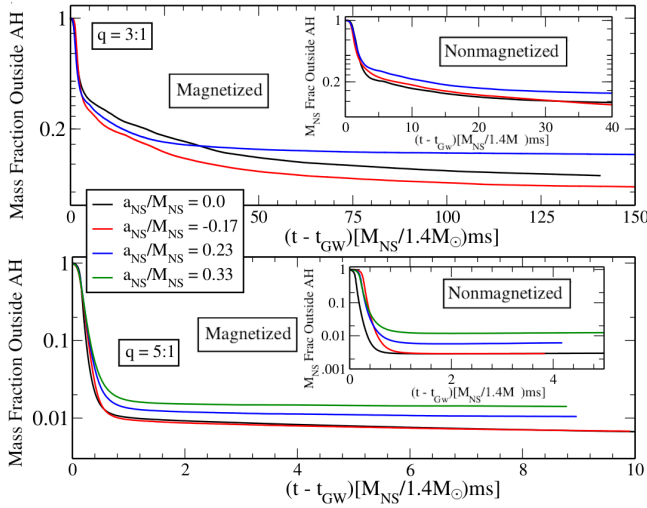


FIG. 5. rest-mass fraction outside the BH apparent horizon as a function of the coordinate time for cases listed in Table II. The insets focus on pure nonmagnetized cases. The coordinate time has been shifted to the merger time t_{mer} .

that eventually overcome the baryon ram pressure of the fall-back debris and drive an outflow collimated by the magnetic field (see bottom panels in Fig. 3 and 4). In Mq3NSm0.17 we find that an incipient jet is launched after $\sim 3500M \simeq 88(M_{\text{NS}}/1.4M_{\odot})$ ms following merger, while in high prograde spin case Mq3NSp0.23 the jet emerges after $\sim 5500M \simeq 138(M_{\text{NS}}/1.4M_{\odot})$ ms. This delay time is not unexpected. As the NS spin increases, the tidal disruption occurs farther out from the ISCO (see Eq. 1) and so more material has larger specific angular momentum and spreads out further. In the prograde NS spin case, the effective ISCO is smaller than in the retrograde case [106]. Thus, a larger fraction of this material remains outside BH horizon and induces a more baryon-loaded environment that survives for a longer time. As a fraction of this material rains back, the matter density above the BH poles drops and the magnetic-field pressure gradients are able to overcome this ram pressure and finally launch a jet. It should be noted that the jet launching may not be possible for all EOSs if the matter fall-back timescale is longer than the disk accretion timescale [66].

We measure the level of the collimation of the jet through the funnel opening angle θ_{jet} defined as the polar angle at which the Poynting flux drops to 50% of its maximum [38]. Based on the angle distribution of the outgoing flux on the surface of a coordinate sphere with radius $60M \sim 455(M_{\text{NS}}/1.4M_{\odot})\text{km}$ (see Fig. 13 in [39]), we estimate that the opening angle of the jet is $\sim 25^{\circ} - 30^{\circ}$.

Following the emergence of the jet, we verify the outgoing material in the funnel has specific energy $E = -u_0 - 1 > 0$ (asymptotic region) and hence is unbound. The characteristic maximum value of the Lorentz factor reached in the outflow is $\Gamma_L \sim 1.2 - 1.3$. However, as pointed out in [112], fluid elements can be accelerated to $\Gamma_L \simeq b^2/2\rho_0 \simeq 100$ (see Table II) consistent with sGRBs which require $\Gamma_L \gtrsim 20$ [113].

Fig. 6 shows the outgoing EM (Poynting) luminosity computed through $L_{\text{Poynt}} \equiv -\int T_t^{r(EM)} \sqrt{-g} dS$ [107] across a spherical surface of coordinate radius $r = 80M \simeq 606(M_{\text{NS}}/1.4M_{\odot})\text{km}$. The luminosity is $L_{\text{Poynt}} \simeq 10^{51.5 \pm 0.5} \text{ergs/s}$ (see Table II), and hence is consistent with the BZ luminosity $L_{\text{BZ}} \sim 10^{51} a^2 B_{15}^2 M_5^2 \text{erg/s}$ (see Eq. 4.50 in [114]), as well as with typical sGRB (equivalent isotropic) luminosities (see e.g. [115]). Here $B_{15} = B/10^{15} \text{G}$ and $a = a_{\text{BH}}/M_{\text{BH}}$ and $M_5 = M_{\text{BH}}/5M_{\odot}$.

To further assess if the BZ mechanism is operating in the BHNS remnants we compute the ratio of the angular velocity of the magnetic fields to the angular velocity of the BH Ω_F (see Eq. 12 in [39]) on a meridional plane passing through the BH centroid and along semicircles of coordinate radii between $r = R_{\text{BH}}$ and $2R_{\text{BH}}$. In all cases Ω_F ranges between $\sim 0.4 - 0.45$ at the BH poles and ~ 0.1 near the equator, and hence the field lines are differentially rotating. It should be noted that deviations from the expected $\Omega_F = 0.5$ value (see e.g. [116]) can be attributed to the deviations from the gauge in which Ω_F is computed (Ω_F is defined for stationary and axisymmetric spacetimes in Killing coordinates), deviation from a split-monopole magnetic field or lack of resolution [38].

We measure the dynamical ejection of matter (ejecta)

through $M_{\text{esc}} = \int \rho_* d^3x$ outside a coordinate radius $r > r_0$, and under the following conditions: a) $E = -1 - u_0 > 0$, and b) positive (outgoing) radial velocity of the ejected material. Here $\rho_* \equiv -\sqrt{\gamma}\rho_0 n_\mu u^\mu$, where γ is the determinant of the three metric and n^μ the future pointing normal vector to a $t = \text{constant}$ hypersurface. To verify that our results are independent of r_0 at large radius, we compute the mass of the ejecta varying r_0 between $30M \simeq 230 (M_{\text{NS}}/1.4M_\odot)$ km and $100M \simeq 760(M_{\text{NS}}/1.4M_\odot)$ km. As shown in the inset of Fig. 6, the initial NS spin has a strong effect on the ejecta (especially in the $q = 5 : 1$ case that we discuss in the next section). The ejecta in Mq3NSp0.23 is around 35% higher than in Mq3NSm0.17, where it turns out to be $10^{-2.1}M_\odot (M_{\text{NS}}/1.4M_\odot)$. Slightly smaller values of the ejecta have been recently reported in BHNS mergers where the NS companion (irrotational) is modeled with softer (H-type) EOSs [117]. Ejecta masses $\gtrsim 10^{-3}M_\odot$ are expected to lead to detectable, transient kilonovae signatures (see e.g. [118]) powered by radioactive decay of unstable elements formed by the neutron-rich material ejected during BHNS mergers [118, 119]. In [120] it was shown that the opacities in r-process ejecta are likely dominated by lanthanides, which induce peak bolometric luminosities for kilonovae of [78]

$$L_{\text{kilnova}} \approx 10^{41} \left(\frac{M_{\text{eje}}}{10^{-2}M_\odot} \right)^{1/2} \left(\frac{v_{\text{eje}}}{0.3c} \right)^{1/2} \text{ erg/s}, \quad (2)$$

and rise times of [78]

$$t_{\text{peak}} \approx 0.25 \left(\frac{M_{\text{eje}}}{10^{-2}M_\odot} \right)^{1/2} \left(\frac{v_{\text{eje}}}{0.3c} \right)^{-1/2} \text{ days}. \quad (3)$$

Here v_{eje} and M_{eje} are the mass-averaged velocity and rest-mass of the ejecta. Using the above equations, we estimate that the bolometric luminosity of potential kilonovae signals is $L_{\text{kilnova}} = 10^{41.3 \pm 0.1} \text{ erg/s}$ with rise times of 0.18 – 0.27 days (see Table II). These luminosities correspond to an R band magnitude of ~ 24 mag at 200 Mpc (inside the aLIGO volume [121]), and above the LSST survey sensitivity of 24.5 mag [78, 120], and hence may be detectable by the LSST survey.

Finally, we compute the characteristic interior temperature T_{disk} of the disk remnant assuming that the specific thermal energy density ϵ_{th} can be modeled as [105]

$$\epsilon_{\text{th}} = \frac{3 k_B T_{\text{disk}}}{2 m_n} + f_s \frac{a T_{\text{disk}}^4}{\rho_0}, \quad (4)$$

where k_B is the Boltzmann constant, m_n is the mass of a nucleon, and $a = 8\pi^5 k_B^4 / (15 h_P^3)$ is the radiation constant. Here h_P is the Planck constant. As pointed out in [105], the first term in Eq. 4 is approximately the thermal energy of the nucleons, while the second represents the thermal energy due to radiation and thermal relativistic particles. The factor f_s accounts for the number of species of ultrarelativistic particles that contribute to thermal energy. When $T \ll 10^{10}$ K thermal radiation is dominated by photons and $f_s = 1$. When $T \gg 10^{10}$ K, electrons and positrons become ultrarelativistic and also contribute to radiation, and hence $f_s = 1 + 2 \times (7/8) = 11/4$.

At sufficiently high temperatures ($T \gtrsim 10^{11}$ K) and densities ($\rho_0 \gtrsim 10^{12} \text{ g/cm}^3$), thermal neutrinos and antineutrinos are copiously generated and become trapped. Taking into account three flavors of neutrinos and antineutrinos $f_s = 11/4 + 3 \times (7/8) = 43/8$.

We measure the thermal energy generated by shocks through the ratio $K = P/P_{\text{cold}}$ (entropy parameter), where $P_{\text{cold}} = \kappa \rho_0^\Gamma$ is the pressure associated with the cold EOS used to build our initial configurations. In all cases we find the characteristic value of the entropy parameter in the disk is $K \sim 200$. Next, we compute the specific thermal energy as $\epsilon_{\text{th}} = (K - 1) \epsilon_{\text{cold}}$ with $\epsilon_{\text{cold}} = \kappa \rho_0$ for a polytropic EOS with $\Gamma = 2$ (see Eq. 12 in [105]). Plugging these values in Eq. 4, we find the characteristic value of the temperature in the disk is $T_{\text{disk}} \sim 10^{11.0}$ K (or 8.6 MeV) for the nonmagnetized cases, where the characteristic densities in the disk are $\rho_0 \sim 10^{12} \text{ gm/cm}^3$ (see bottom panels in Fig. 2), and $T \sim 10^{10.6}$ K (or 3.4 MeV) for the magnetized cases, where the characteristic densities are $\rho_0 \sim 10^{11} \text{ gm/cm}^3$ (see bottom panels in Figs. 3 and 4). Thus, these hot accretion disks may emit a copious amount of neutrinos with a peak luminosity of 10^{53} erg/s through thermal pair production and subsequent electron/positron captures on free nucleons [75]. However, their lifetimes might be too small to explain the majority of sGRBs [74]. It has been suggested that BH + disk engines that power typical sGRBs may be dominated initially by thermal pair production followed by the BZ process, leading to a transition from a thermally dominated fireball to a Poynting dominated outflow as observed in some GRBs, such as GRB 160625B [76].

Figure 7 shows the GW strain h_+ of the dominant mode (2, 2) for these configurations. Left column displays the nonmagnetized evolutions, while the right one displays the magnetized evolutions. The corresponding binaries (nonmagnetized and magnetized) merge roughly at the same time (here the merger time t_{mer} is defined as the time of peak amplitude of the GWs). This result is anticipated because the seed magnetic field is dynamically weak and there is no significant enhancement of its magnitude during the inspiral (the seed magnetic field is simply advected with the fluid). However, due to the hang-up effect [122], the prograde NS spin configuration ($a_{\text{NS}}/M_{\text{NS}} = 0.23$) aligned with the total orbital angular momentum of the system (bottom panel in Fig. 7) undergoes about one or two more orbits compared to the irrotational and the retrograde NS spin ($a_{\text{NS}}/M_{\text{NS}} = -0.17$) cases (top and middle panels), respectively. A similar effect has been reported in BBHs [122], and BNSs [94, 107, 123–126].

B. Mass ratio $q = 5 : 1$

Fig. 8 summarizes the evolution of Mq5NSp0.33 (our extreme case). All configurations with mass ratio $q = 5 : 1$ in Table II have basically the same fate independent of the magnitude of the magnetic field or the initial NS spin: The tidal disruption occurs closer to the ISCO, resulting in short tidal tails (see middle panel) that leave stellar debris outside the BH horizon with mass $\lesssim 1.4\%$ of the rest-mass of the NS

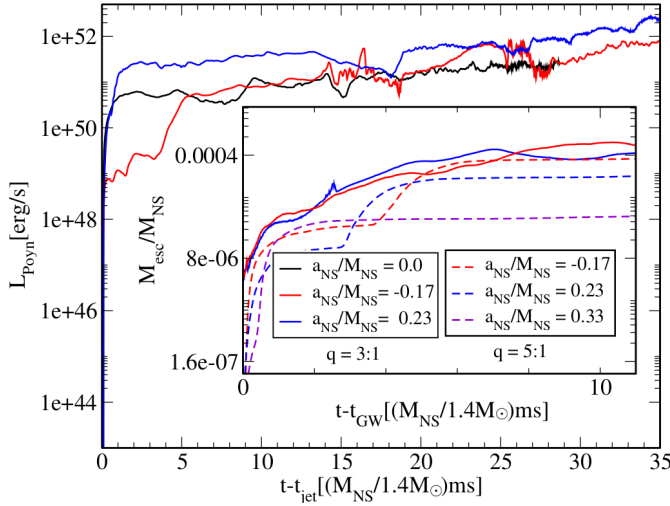


FIG. 6. Outgoing EM (Poynting) luminosity following jet launching, computed on a coordinate sphere of radius $r = 80M \simeq 606(M_{\text{NS}}/1.4M_{\odot})$ km for the magnetized cases listed in Table II. The inset shows the rest-mass fraction of escaping matter following the peak amplitude of GWs.

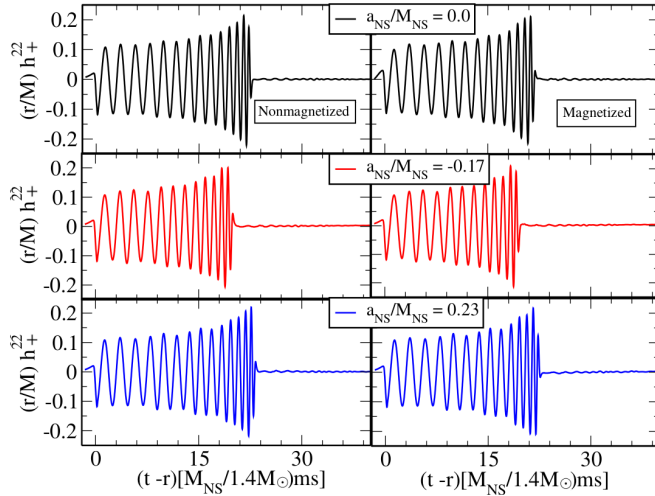


FIG. 7. Mode $(l, m) = (2, 2)$ of the GW strain h_+ as function of the retarded time extracted at a coordinate sphere of radius $r = 80M \simeq 606(M_{\text{NS}}/1.4M_{\odot})$ km for nonmagnetized (left column) and magnetized (right column) cases with mass ratio $q = 3 : 1$ (see Table II).

(bottom panel of Fig. 5). See Table II for other cases. We do not find evidence for an outflow or large-scale magnetic field collimation (see bottom panel in Fig. 8).

Bottom panel of Fig. 5 shows the rest-mass fraction outside the BH horizon. We observe that in Mq5NSp0.33 the mass outside the BH horizon is around three times larger than in Mq5NSm0.17. So, the higher the prograde NS spin, the larger the fraction of matter ejected. The inset of Fig. 6 shows the dynamical ejection of matter for the magnetized cases (similar values are found for the nonmagnetized cases). In the extreme cases, the ejecta ranges

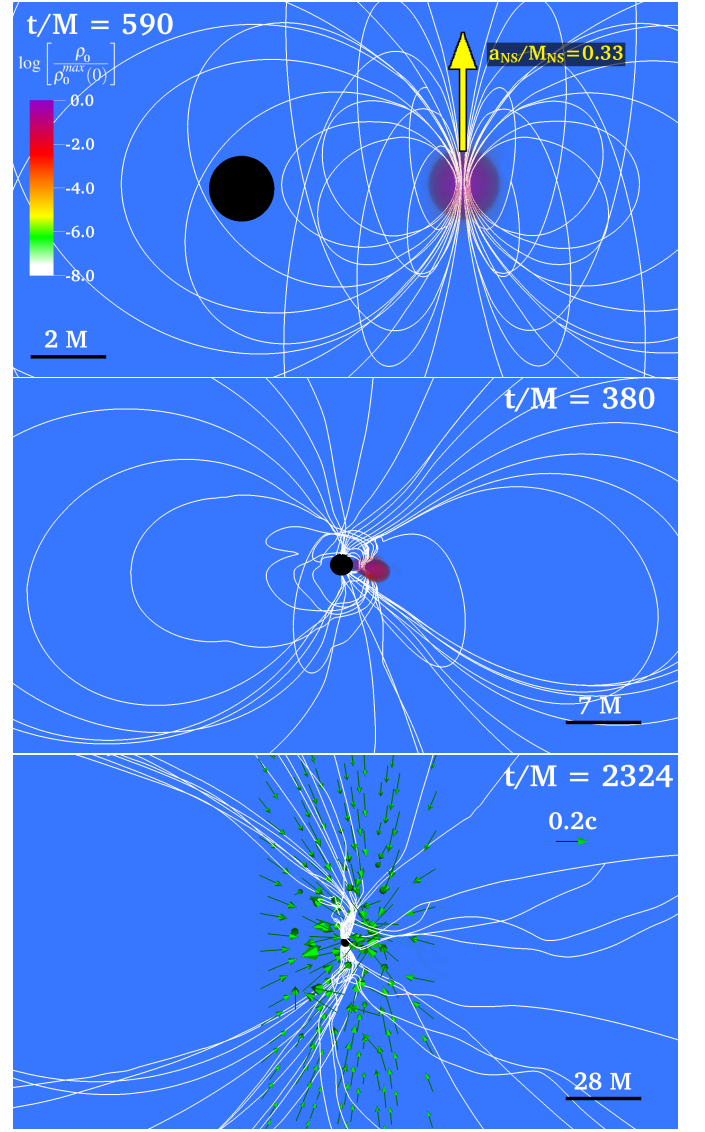


FIG. 8. Same as Fig. 3 but for Mq5NSp0.33.

between $10^{-4.5}M_{\odot}(M_{\text{NS}}/1.4M_{\odot})$ (for Mq5NSm0.17) and $10^{-3.5}M_{\odot}(M_{\text{NS}}/1.4M_{\odot})$ (for Mq5NSp0.33). The latter is near the threshold value of ejecta required to give rise to a detectable kilonova [118]. Using Eqs. 2 and 3 we estimate peak bolometric luminosities from potential kilonovae of $L_{\text{kilnova}} \sim 10^{40.0} - 10^{40.6}$ erg/s and rise times $\lesssim 1$ h (see Table II). Such a kilonova is potentially detectable by the LSST survey, although it would require rapid response and high cadence EM follow-up observations. These results suggest that even in the absence of a jet, the GWs from BHNS mergers with moderate mass ratio and/or moderate BH spin may be accompanied by detectable kilonovae signatures if the companion is a highly spinning NS, which agrees with [78].

The GW strain h_+ of the dominant mode $(l, m) = (2, 2)$ for the nonmagnetized (left column) and magnetized (right column) evolutions is shown in Fig. 9. We observe that the more extreme configurations ($a_{\text{NS}}/M_{\text{NS}} = 0.23$ and $a_{\text{NS}}/M_{\text{NS}} =$

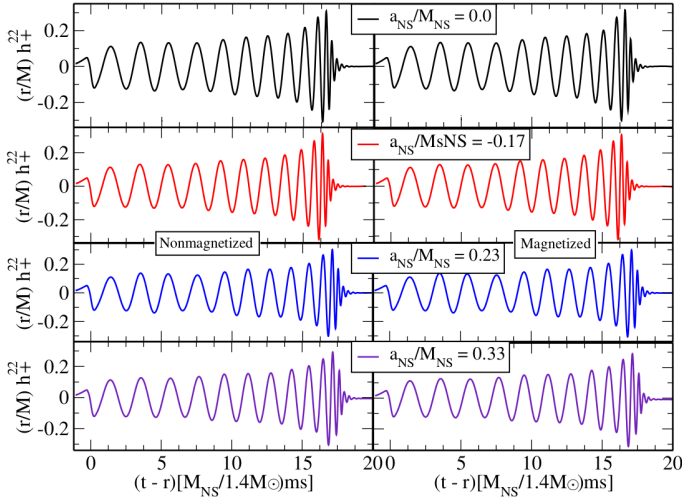


FIG. 9. Same as Fig. 7 but for BHNS configuration with mass ratio $q = 5 : 1$ (see Table II).

0.33) displayed on the two bottom rows undergo about half an orbit ($a_{\text{NS}}/M_{\text{NS}} = 0.23$) and a full orbit ($a_{\text{NS}}/M_{\text{NS}} = 0.33$) more compared to the nonspinning and retrograde NS spin cases (first two rows). Thus, NS spin can lead to dephasing and should be accounted for in BHNS waveform templates.

C. Distinguishability of the gravitational waves

As mentioned in the previous section, as the initial NS spin increases, the binary inspiral lasts longer, resulting in more gravitational wave cycles (see Figs. 7 and 9). This enhancement induces a dephasing with respect to the non-spinning cases, and a change in the amplitude of the GWs of $\lesssim 5\%$ between the respective waveforms, which is reflected in slight changes in the energy ΔE_{GW} and angular momentum ΔJ_{GW} carried away by GWs (see Table II), as well as in the kick velocity v_{kick} due to recoil (see Eqs. 3.7 and 3.20 in [128]). In this section, we probe if these spin-driven and magnetic effects can be distinguished by aLIGO.

We start by extending the GW spectra in the frequency domain, creating a hybrid waveform. Following [65], we append a TaylorT1 post-Newtonian waveform [129] to that of our numerical relativity simulations. The hybrid waveform is then obtained by minimizing

$$\int_{t_i}^{t_f} dt [(h_+^{\text{NR}} - h_+^{\text{PN}})^2 + (h_x^{\text{NR}} - h_x^{\text{PN}})^2]^{1/2}, \quad (5)$$

via the Nelder-Mead algorithm [130], using as free parameters the initial PN phase, amplitude, and orbital angular frequency. In cases with mass ratio $q = 3 : 1$ we integrate the above expression between $t_i = 150M$ and $t_f = 450M$, while in cases with mass ratio $q = 5 : 1$ the integration range is between $t_i = 150M$ and $t_f = 250M$.

Fig. 10 shows the GW spectrum of the dominant mode $(l, m) = (2, 2)$ at a source distance of 100Mpc for our ex-

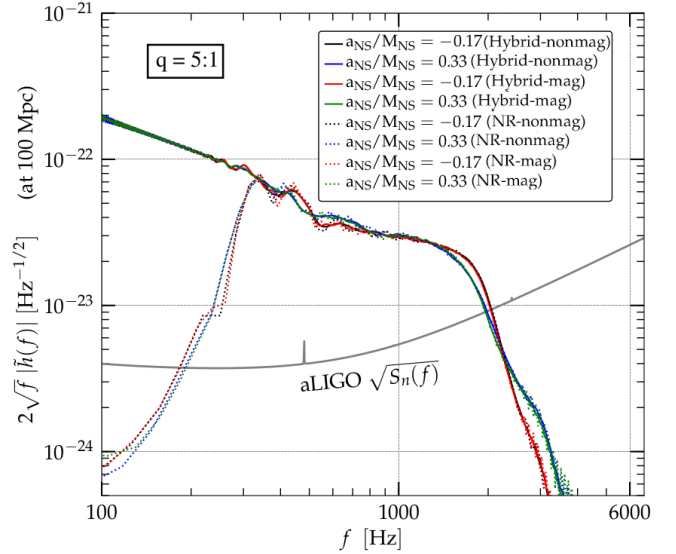
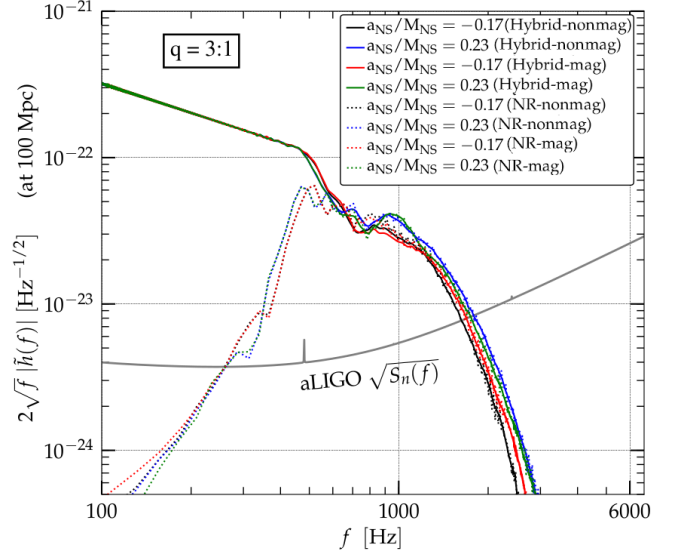


FIG. 10. Gravitational-wave power spectrum of the dominant mode $(l, m) = (2, 2)$ at a source distance of 100Mpc for our extreme cases with mass ratio $q = 3 : 1$ (top panel) and mass ratio $q = 5 : 1$ (bottom panel), along with the aLIGO noise curve. This curve corresponds to the ZERO_DET_HIGH_P configuration [127]. Solid curves display the hybrid waveform found by appending the TaylorT1 PN waveform to the raw numerical signal (dotted curves).

treme cases listed in Table II, along with the aLIGO noise curve of the ZERO_DET_HIGH_P configuration [127]. Solid (dotted) lines display the hybrid (raw numerical) signals. We observe that the GW spectrum for cases with mass ratio $q = 3 : 1$ (top panel) rapidly decays as the star becomes disrupted ($f \sim 900 (M_{\text{NS}}/1.4M_{\odot})^{-1}$ Hz). By contrast, in cases with mass ratio $q = 5 : 1$ (bottom panel), the signal slowly decays until merger, where the star basically plunges into the BH ($f \sim 1700 (M_{\text{NS}}/1.4M_{\odot})^{-1}$ Hz), and then the GW power

drops significantly. Unlike the NS spin imprints on the GWs evident at high frequencies, the magnetic field imprints are not significant. In the lowest mass ratio cases, the differences in the GW spectrum are marginally observable in the aLIGO band (top panel), while on those with mass ratio $q = 5 : 1$ are not evident at all even outside the aLIGO band (bottom panel).

A more precise way to assess the distinguishability is through the match function \mathcal{M}_{GW} defined as [131]

$$\mathcal{M}_{\text{GW}} = \max_{(\phi_c, t_c)} \frac{\langle h_1 | h_2(\phi_c, t_c) \rangle}{\sqrt{\langle h_1 | h_1 \rangle \langle h_2 | h_2 \rangle}}, \quad (6)$$

between two given waveforms. The maximization is taken over a large set of phase shifts ϕ_c and time shifts t_c . Here $\langle h_1 | h_2 \rangle$ denotes the noise-weighted inner product [131]

$$\langle h_1 | h_2 \rangle = 4 \text{Re} \int_0^\infty \frac{\tilde{h}_1(f) \tilde{h}_2^*(f)}{S_h(f)} df, \quad (7)$$

were $h = h_+ - i h_\times$, \tilde{h} is the Fourier transform of the strain amplitude $\sqrt{\tilde{h}_+(f)^2 + \tilde{h}_\times(f)^2}$ of the dominant mode $(l, m) = (2, 2)$, and $S_h(f)$ is the power spectral density of the aLIGO noise [127]. In our extreme cases, we find that $\mathcal{M}_{\text{GW}} = 0.9980$ between the waveforms of the q3NSm0.17 cases, and $\mathcal{M}_{\text{GW}} = 0.9982$ between those of the q3NSp0.23. Similarly, $\mathcal{M}_{\text{GW}} = 0.9998$ for all of our extreme cases with mass ratio $q = 5 : 1$.

The standard choice for the threshold match for distinguishing two signals is $1 - 1/(2\rho^2)$, where ρ here is the signal-to-noise ratio (SNR). For a SNR of 15 [132], two signals are distinguishable when $\mathcal{M}_{\text{GW}} \gtrsim 0.9956$. Using Equation (18) in [133] (with one degree of freedom since we compare configurations varying one parameter), a match of $1 - 1/(2\rho^2)$ corresponds to a 68% confidence level. Thus, it seems unlikely that aLIGO detectors can detect the magnetic field imprints on the GWs even at 68% confidence level. By contrast, the imprints of the NS spin on the waveform are more easily detectable. The match function between the waveform of Mq3NSp0.23 and Mq3NSm0.17 is 0.9844, and 0.9874 between those of Mq5NSp0.33 and Mq5NSm0.17, and hence smaller than the threshold match value.

IV. CONCLUSIONS

We previously reported self-consistent MHD numerical simulations in full GR showing that BHNS binaries undergoing merger and significant NS tidal disruption outside the ISCO can launch a magnetically-driven jet [38, 39]. This happens whenever a net poloidal magnetic flux is accreted onto the BH with $B^2/8\pi\rho_0 \gg 1$ above the BH poles, and hence these systems serve as a possible progenitor of the central engine that powers a sGRB. However, population synthesis studies [58, 134] along with the reported aLIGO/Virgo GW detections [2, 5, 6] suggest that in typical BHNSs we may have $M_{\text{BH}}/M_{\text{NS}} \gtrsim 5$. For such high mass ratios the NS companion simply plunges into the BH before undergoing tidal disruption, leaving a negligible amount of matter outside the BH

horizon ($\lesssim 2\%$ of the NS rest-mass). Thus, BHNS mergers may not be accompanied by a near simultaneous, observable EM counterpart. However, the NS spin can have a strong impact on the dynamical ejection of matter, and so may lead to subsequent kilonovae signatures. It should be noted that the current GW observations set constraints on the effective spin of the binary but not on the individual spins.

In this paper, we explored the impact of the NS spin companion on the dynamical ejection of matter, the mass of the accretion disk, and the jet launching, from BHNS binaries undergoing merger with moderate mass ratios ($q = 3 : 1$ and $q = 5 : 1$). For comparative purposes, we considered the quasiequilibrium BHNS initial data used previously in [39, 105] and endowed the NS companion with an effective spin [93].

Consistent with our previous results [38, 39], we found that all magnetized cases with mass ratio $q = 3 : 1$ in Table II launch a magnetically-driven jet after $\Delta t \sim 3500M - 5500 \approx 88 - 138(M_{\text{NS}}/1.4M_\odot) \text{ ms}$ following the peak GW signal (see bottom panels in Figs. 3 and 4). At these times the force-free parameter above the poles of the BH reaches values of $b^2/(2\rho_0) \gtrsim 100$ (see Table II). The time delay between GW peak and jet launching depends strongly on the NS spin. The larger the NS spin, the longer the delay. This result can be explained by the fact that as the prograde NS spin increases the effective ISCO [106] decreases, while the NS becomes less bound, so that the onset of NS tidal disruption occurs farther out from the ISCO. This causes long tidal tails of matter having larger specific angular momentum that spread out and form a baryon-loaded environment that persists for a longer time. The lifetime of the jet [$\Delta t \sim 0.5 - 0.8(M_{\text{NS}}/1.4M_\odot) \text{ s}$] and outgoing Poynting luminosity [$L_{\text{Poynt}} \sim 10^{51.5 \pm 0.5} \text{ erg/s}$] are consistent with typical sGRBs, as well as with the BZ mechanism [71]. Consistent with our previous results [38, 39], we estimated that the opening angle of the jet is $\sim 25^\circ - 30^\circ$. In contrast to the $q = 3 : 1$ cases, we do not find evidence of outflow or large-scale magnetic field collimation in any of the BHNS cases with mass ratio $q = 5 : 1$, (see bottom panel in Fig. 8). Persistent fall-back debris in the atmosphere are observed until the termination of our simulations.

We estimated the characteristic interior temperature of the disk remnant via Eq. 4, and found that it is $T_{\text{disk}} \sim 10^{11} \text{ K}$ (or 8.6 MeV). Thus, it may emit a copious amount of neutrinos with peak luminosity of 10^{53} erg/s [75]. It has been suggested that, as neutrino annihilation may carry away a significant amount of energy from inner regions of the disk, it may help the jet development. Thus, a BH + disk remnant that powers a typical sGRB may be dominated initially by thermal pair production followed by the BZ process [76].

We observed that the dynamical ejection of matter is strongly affected by the initial NS spin. The ejecta ranges between $\sim 10^{-4.5}(M_{\text{NS}}/1.4M_\odot)M_\odot$ and $\sim 10^{-2}(M_{\text{NS}}/1.4M_\odot)M_\odot$, and may induce kilonovae signatures with peak bolometric luminosities of $L_{\text{kno}} \sim 10^{40} - 10^{41.4} \text{ erg/s}$ and rise times $\lesssim 6.5 \text{ h}$, potentially detectable by the LSST survey [77]. These preliminary results suggest that moderately high-mass ratio BHNS binaries under-

going merger, where the NS companion has a significant spin, may give rise to a detectable kilonovae signatures even if a magnetically-driven jet is absent.

Furthermore, we probed if magnetic-field and NS spin imprints on the GWs can be distinguished by aLIGO. To assess this possibility, we stitched a TaylorT1 Post-Newtonian waveform to that of our numerical simulations. Next, we computed the GW power spectrum and the match function \mathcal{M}_{GW} (see Eq. 6). Unlike the NS spin imprints on the GWs evident at high frequencies (see Fig. 10), we found that in the lowest mass ratio cases, the GW power spectrum of the corresponding nonmagnetized and magnetized signals differ marginally inside the aLIGO band, while for those with mass ratio $q = 5 : 1$, the differences are negligible even outside the aLIGO band. The match function for our extreme cases is $\mathcal{M}_{\text{GW}} = 0.9980$ between the waveforms of q3NSm0.17 cases, and $\mathcal{M}_{\text{GW}} = 0.9982$ between those of q3NSp0.23. Similarly, $\mathcal{M}_{\text{GW}} = 0.9998$ for all of our extreme case with mass ratio $q = 5 : 1$. It appears unlikely that aLIGO detectors can detect magnetic-field imprints on the GWs which require $\mathcal{M}_{\text{GW}} \lesssim 0.9956$ for a signal-to-noise ratio of 15 [132]. By contrast, the imprints of the NS spin on the waveform are more easily detectable. The match function between the waveform of Mq3NSp0.23 and Mq3NSm0.17 is 0.9844, and 0.9874 between those of Mq5NSp0.33 and Mq5NSm0.17.

Notice that due to the finite computational resources at our disposal, we explored only two extreme cases to probe the impact of the NS spin on the dynamical ejection of matter when the NS is (or is not) tidally disrupted before merger. Our motivation for considering a non-spinning BH in the $q = 5 : 1$ case was to observe if the NS spin alone can change the amount of mass left outside the BH horizon. Using the fitting model in [61] (which applies to non-spinning BHs) for a BHNSs with mass ratio $q = 5 : 1$, a BH spin larger than 0.6 is required to tidally disrupt the NS before merger and to leave matter outside the BH. Thus, by considering a worst case scenario for ejecta and matter outside the BH we can study the

NS spin effects alone. We will explore more general cases in the future.

Finally, some caveats are in order. Despite the fact that our initial data with NS spin slightly violate the constraints, as the evolution proceeds our efficient constraint damping scheme decreases the constraint violations down to the same levels as our constraint-satisfying initial data with irrotational neutron stars. However, some of the reported results in this work may be affected by the fact that our method for endowing the NS with spin throws the NS slightly off equilibrium for the highest spin values we consider. While the trends with NS spin we reported are robust against this property of our initial data, given that they are supported by analytic arguments, the precise values of ejecta and disk masses we reported could be affected. We plan to address these points in future work.

ACKNOWLEDGMENTS

We thank the Illinois Relativity group REU team (K. Nelli, M. N.T. Nguyen, and S. Qunell) for assistance with some of the visualizations. This work was supported by NSF Grants No. PHY-1662211 and No. PHY-2006066, and NASA Grant No. 80NSSC17K0070 to the University of Illinois at Urbana-Champaign, and NSF Grant PHY-1912619 to the University of Arizona. This work made use of the Extreme Science and Engineering Discovery Environment (XSEDE), which is supported by National Science Foundation Grant No. TG-MCA99S008. This research is also part of the Frontera computing project at the Texas Advanced Computing Center. Frontera is made possible by National Science Foundation award OAC-1818253. Resources supporting this work were also provided by the NASA High-End Computing (HEC) Program through the NASA Advanced Supercomputing (NAS) Division at Ames Research Center.

-
- [1] B. Abbott *et al.* (LIGO Scientific, Virgo), *Phys. Rev. X* **9**, 031040 (2019), [arXiv:1811.12907 \[astro-ph.HE\]](#).
 - [2] B. P. Abbott *et al.* (Virgo, LIGO Scientific), *Phys. Rev. Lett.* **119**, 161101 (2017), [arXiv:1710.05832 \[gr-qc\]](#).
 - [3] H. Yang, W. E. East, and L. Lehner, *Astrophys. J.* **856**, 110 (2018), [arXiv:1710.05891 \[gr-qc\]](#).
 - [4] T. Hinderer *et al.*, (2018), [arXiv:1808.03836 \[astro-ph.HE\]](#).
 - [5] GW alerts, “[Ligo/virgo o3 public alerts](#),”.
 - [6] R. Abbott *et al.* (LIGO Scientific, Virgo), (2020), [arXiv:2010.14527 \[gr-qc\]](#).
 - [7] T. M. Tauris *et al.*, *Astrophys. J.* **846**, 170 (2017), [arXiv:1706.09438 \[astro-ph.HE\]](#).
 - [8] I. Mandel, C.-J. Haster, M. Dominik, and K. Belczynski, *Mon. Not. Roy. Astron. Soc.* **450**, L85 (2015), [arXiv:1503.03172 \[astro-ph.HE\]](#).
 - [9] T. B. Littenberg, B. Farr, S. Coughlin, V. Kalogera, and D. E. Holz, *Astrophys. J.* **807**, L24 (2015), [arXiv:1503.03179 \[astro-ph.HE\]](#).
 - [10] A. Tsokaros, M. Ruiz, S. L. Shapiro, L. Sun, and K. Uryū, *Phys. Rev. Lett.* **124**, 071101 (2020), [arXiv:1911.06865 \[astro-ph.HE\]](#).
 - [11] R. Abbott *et al.* (LIGO Scientific, Virgo), *Astrophys. J.* **896**, L44 (2020), [arXiv:2006.12611 \[astro-ph.HE\]](#).
 - [12] A. Tsokaros, M. Ruiz, and S. L. Shapiro, (2020), [arXiv:2007.05526 \[astro-ph.HE\]](#).
 - [13] E. R. Most, L. J. Papenfort, L. R. Weih, and L. Rezzolla, (2020), [arXiv:2006.14601 \[astro-ph.HE\]](#).
 - [14] D. A. Godzieba, D. Radice, and S. Bernuzzi, (2020), [arXiv:2007.10999 \[astro-ph.HE\]](#).
 - [15] I. Tews, P. T. Pang, T. Dietrich, M. W. Coughlin, S. Antier, M. Bulla, J. Heinzl, and L. Issa, (2020), [arXiv:2007.06057 \[astro-ph.HE\]](#).
 - [16] H. T. Cromartie *et al.*, *Nature Astron.* **4**, 72 (2019), [arXiv:1904.06759 \[astro-ph.HE\]](#).
 - [17] J. A. Orosz, J. E. McClintock, R. A. Remillard, and S. Corbel, *Astrophys. J.* **616**, 376 (2004), [arXiv:astro-ph/0404343 \[astro-ph\]](#).

- [18] C. V. et al., *The Astrophysical Journal Letters* **826**, L6 (2016).
- [19] V. Connaughton *et al.*, *Astrophys. J. Lett.* **853**, L9 (2018), [arXiv:1801.02305 \[astro-ph.HE\]](#).
- [20] B. P. Abbott, R. Abbott, T. D. Abbott, F. Acernese, K. Ackley, C. Adams, T. Adams, P. Addesso, R. X. Adhikari, V. B. Adya, and *et al.*, *Physical Review Letters* **118**, 221101 (2017), [arXiv:1706.01812 \[gr-qc\]](#).
- [21] F. Verrecchia *et al.* (AGILE), *Astrophys. J. Lett.* **847**, L20 (2017), [arXiv:1706.00029 \[astro-ph.HE\]](#).
- [22] B. P. Abbott *et al.*, *Astrophys. J.* **848**, L12 (2017), [arXiv:1710.05833 \[astro-ph.HE\]](#).
- [23] B. P. Abbott *et al.* (Virgo, Fermi-GBM, INTEGRAL, LIGO Scientific), *Astrophys. J.* **848**, L13 (2017), [arXiv:1710.05834 \[astro-ph.HE\]](#).
- [24] B. P. Abbott *et al.* (Virgo, LIGO Scientific), *Astrophys. J.* **850**, L39 (2017), [arXiv:1710.05836 \[astro-ph.HE\]](#).
- [25] R. Chornock *et al.*, *Astrophys. J.* **848**, L19 (2017), [arXiv:1710.05454 \[astro-ph.HE\]](#).
- [26] P. S. Cowperthwaite *et al.*, *Astrophys. J.* **848**, L17 (2017), [arXiv:1710.05840 \[astro-ph.HE\]](#).
- [27] D. Kasen, B. Metzger, J. Barnes, E. Quataert, and E. Ramirez-Ruiz, *Nature* (2017), 10.1038/nature24453, [Nature551,80(2017)], [arXiv:1710.05463 \[astro-ph.HE\]](#).
- [28] M. Nicholl *et al.*, *Astrophys. J.* **848**, L18 (2017), [arXiv:1710.05456 \[astro-ph.HE\]](#).
- [29] S. Valenti, D. J. Sand, S. Yang, E. Cappellaro, L. Tartaglia, A. Corsi, S. W. Jha, D. E. Reichart, J. Haislip, and V. Kouprianov, *Astrophys. J.* **848**, L24 (2017), [arXiv:1710.05854 \[astro-ph.HE\]](#).
- [30] V. Paschalidis, K. Yagi, D. Alvarez-Castillo, D. B. Blaschke, and A. Sedrakian, *Phys. Rev. D* **97**, 084038 (2018), [arXiv:1712.00451 \[astro-ph.HE\]](#).
- [31] R. Essick, P. Landry, and D. E. Holz, *Phys. Rev. D* **101**, 063007 (2020), [arXiv:1910.09740 \[astro-ph.HE\]](#).
- [32] B. Paczynski, *Astrophys. J.* **308**, L43 (1986).
- [33] D. Eichler, M. Livio, T. Piran, and D. N. Schramm, *Nature (London)* **340**, 126 (1989).
- [34] R. Narayan, B. Paczynski, and T. Piran, *Astrophys. J. Letters* **395**, L83 (1992).
- [35] M. Ruiz, R. N. Lang, V. Paschalidis, and S. L. Shapiro, *Astrophys. J.* **824**, L6 (2016).
- [36] M. Ruiz and S. L. Shapiro, *Phys. Rev. D* **96**, 084063 (2017), [arXiv:1709.00414 \[astro-ph.HE\]](#).
- [37] M. Ruiz, A. Tsokaros, and S. L. Shapiro, *Phys. Rev. D* **101**, 064042 (2020), [arXiv:2001.09153 \[astro-ph.HE\]](#).
- [38] V. Paschalidis, M. Ruiz, and S. L. Shapiro, *Astrophys. J.* **806**, L14 (2015), [arXiv:1410.7392 \[astro-ph.HE\]](#).
- [39] M. Ruiz, S. L. Shapiro, and A. Tsokaros, *Phys. Rev. D* **98**, 123017 (2018), [arXiv:1810.08618 \[astro-ph.HE\]](#).
- [40] B. Margalit and B. D. Metzger, *Astrophys. J.* **850**, L19 (2017), [arXiv:1710.05938 \[astro-ph.HE\]](#).
- [41] M. Shibata, S. Fujibayashi, K. Hotokezaka, K. Kiuchi, K. Kyutoku, Y. Sekiguchi, and M. Tanaka, *Phys. Rev. D* **96**, 123012 (2017), [arXiv:1710.07579 \[astro-ph.HE\]](#).
- [42] M. Ruiz, S. L. Shapiro, and A. Tsokaros, *Phys. Rev. D* **97**, 021501 (2018), [arXiv:1711.00473 \[astro-ph.HE\]](#).
- [43] L. Rezzolla, E. R. Most, and L. R. Weih, *Astrophys. J.* **852**, L25 (2018), [Astrophys. J. Lett.852,L25(2018)], [arXiv:1711.00314 \[astro-ph.HE\]](#).
- [44] E. R. Most, L. R. Weih, L. Rezzolla, and J. Schaffner-Bielich, *Phys. Rev. Lett.* **120**, 261103 (2018), [arXiv:1803.00549 \[gr-qc\]](#).
- [45] B. P. Abbott *et al.* (Virgo, LIGO Scientific), (2018), [arXiv:1805.11581 \[gr-qc\]](#).
- [46] D. Radice, A. Perego, F. Zappa, and S. Bernuzzi, *Astrophys. J.* **852**, L29 (2018), [arXiv:1711.03647 \[astro-ph.HE\]](#).
- [47] A. Bauswein, O. Just, H.-T. Janka, and N. Stergioulas, *Astrophys. J.* **850**, L34 (2017), [arXiv:1710.06843 \[astro-ph.HE\]](#).
- [48] C. Raithel, F. Özel, and D. Psaltis, *Astrophys. J. Lett.* **857**, L23 (2018), [arXiv:1803.07687 \[astro-ph.HE\]](#).
- [49] C. A. Raithel and F. Özel, (2019), 10.3847/1538-4357/ab48e6, [arXiv:1908.00018 \[astro-ph.HE\]](#).
- [50] C. A. Raithel, *Eur. Phys. J. A* **55**, 80 (2019), [arXiv:1904.10002 \[astro-ph.HE\]](#).
- [51] L. Baiotti, *Prog. Part. Nucl. Phys.* **109**, 103714 (2019), [arXiv:1907.08534 \[astro-ph.HE\]](#).
- [52] C. Horowitz, *Annals Phys.* **411**, 167992 (2019), [arXiv:1911.00411 \[astro-ph.HE\]](#).
- [53] A. Guerra Chaves and T. Hinderer, *J. Phys. G* **46**, 123002 (2019), [arXiv:1912.01461 \[nucl-th\]](#).
- [54] D. Radice, S. Bernuzzi, and A. Perego, (2020), 10.1146/annurev-nucl-013120-114541, [arXiv:2002.03863 \[astro-ph.HE\]](#).
- [55] K. Chatziioannou, *Gen. Rel. Grav.* **52**, 109 (2020), [arXiv:2006.03168 \[gr-qc\]](#).
- [56] M. J. Graham, K. E. S. Ford, B. McKernan, N. P. Ross, D. Stern, K. Burdge, M. Coughlin, S. G. Djorgovski, A. J. Drake, D. Duev, M. Kasliwal, A. A. Mahabal, S. van Velzen, J. Belecki, E. C. Bellm, R. Burruss, S. B. Cenko, V. Cunningham, G. Helou, S. R. Kulkarni, F. J. Masci, T. Prince, D. Reiley, H. Rodriguez, B. Rusholme, R. M. Smith, and M. T. Soumagnac, *Phys. Rev. Lett.* **124**, 251102 (2020).
- [57] A. Pozanenko, P. Y. Minaev, S. Grebenev, and I. Chelovekov, *Astron. Lett.* **45**, 710 (2020), [arXiv:1912.13112 \[astro-ph.HE\]](#).
- [58] K. Belczynski, R. E. Taam, E. Rantsiou, and M. van der Sluys, *Astrophys. J.* **682**, 474 (2008), [arXiv:astro-ph/0703131 \[ASTRO-PH\]](#).
- [59] K. Belczynski, M. Dominik, T. Bulik, R. O’Shaughnessy, C. Fryer, and D. Holz, *Astrophys. J.* **715**, L138 (2010), [arXiv:1004.0386 \[astro-ph.HE\]](#).
- [60] N. Giacobbo and M. Mapelli, *Mon. Not. Roy. Astron. Soc.* **480**, 2011 (2018), [arXiv:1806.00001 \[astro-ph.HE\]](#).
- [61] F. Foucart, *Phys. Rev. D* **86**, 124007 (2012), [arXiv:1207.6304 \[astro-ph.HE\]](#).
- [62] F. Foucart, T. Hinderer, and S. Nissanke, *Phys. Rev. D* **98**, 081501 (2018), [arXiv:1807.00011 \[astro-ph.HE\]](#).
- [63] F. Foucart, *Front. Astron. Space Sci.* **7**, 46 (2020), [arXiv:2006.10570 \[astro-ph.HE\]](#).
- [64] Z. B. Etienne, J. A. Faber, Y. T. Liu, S. L. Shapiro, K. Taniguchi, and T. W. Baumgarte, *Phys. Rev. D* **77**, 084002 (2008), [arXiv:0712.2460 \[astro-ph\]](#).
- [65] Z. B. Etienne, Y. T. Liu, V. Paschalidis, and S. L. Shapiro, *Phys. Rev. D* **85**, 064029 (2012).
- [66] V. Paschalidis, *Class. Quant. Grav.* **34**, 084002 (2017).
- [67] P. N. Bhat *et al.*, *Astrophys. J. Suppl.* **223**, 28 (2016), [arXiv:1603.07612 \[astro-ph.HE\]](#).
- [68] A. Lien *et al.*, *Astrophys. J.* **829**, 7 (2016), [arXiv:1606.01956 \[astro-ph.HE\]](#).
- [69] D. S. Svinkin, D. D. Frederiks, R. L. Aptekar, S. V. Golenetskii, V. D. Pal’shin, P. P. Oleynik, A. E. Tsvetkova, M. V. Ulanov, T. L. Cline, and K. Hurley, *Astrophys. J. Suppl.* **224**, 10 (2016), [arXiv:1603.06832 \[astro-ph.HE\]](#).
- [70] M. Ajello *et al.*, *Astrophys. J.* **878**, 52 (2019), [arXiv:1906.11403 \[astro-ph.HE\]](#).
- [71] R. D. Blandford and R. L. Znajek, *mnras* **179**, 433 (1977).
- [72] K. S. Thorne, R. H. Price, and D. A. MacDonald, *Black Holes: The Membrane Paradigm* (1986).

- [73] S. L. Shapiro, *Phys. Rev.* **D95**, 101303 (2017), [arXiv:1705.04695 \[astro-ph.HE\]](#).
- [74] O. Just, M. Obergaulinger, H. T. Janka, A. Bauswein, and N. Schwarz, *Astrophys. J.* **816**, L30 (2016).
- [75] K. Kyutoku, K. Kiuchi, Y. Sekiguchi, M. Shibata, and K. Taniguchi, *Phys. Rev. D* **97**, 023009 (2018), [arXiv:1710.00827 \[astro-ph.HE\]](#).
- [76] F. F. Dirirsa (Fermi-LAT), *Proceedings, 4th Annual Conference on High Energy Astrophysics in Southern Africa (HEASA 2016): Cape Town, South Africa, August 25-26, 2016, PoS HEASA2016*, 004 (2017).
- [77] D. Alonso *et al.* (LSST Dark Energy Science), (2018), [arXiv:1809.01669 \[astro-ph.CO\]](#).
- [78] W. E. East, V. Paschalidis, and F. Pretorius, *Astrophys. J.* **807**, L3 (2015), [arXiv:1503.07171 \[astro-ph.HE\]](#).
- [79] K. Taniguchi, T. W. Baumgarte, J. A. Faber, and S. L. Shapiro, *Phys. Rev. D* **74**, 041502 (2006).
- [80] J. W. Hessels, S. M. Ransom, I. H. Stairs, P. C. C. Freire, V. M. Kaspi, and F. Camilo, *Science* **311**, 1901 (2006), [arXiv:astro-ph/0601337](#).
- [81] <http://www.cactuscode.org/>.
- [82] E. Schnetter, S. H. Hawley, and I. Hawke, *Class. Quantum Grav.* **21**, 1465 (2004), [arXiv:gr-qc/0310042](#).
- [83] M. Shibata and T. Nakamura, *Phys. Rev. D* **52**, 5428 (1995).
- [84] T. W. Baumgarte and S. L. Shapiro, *Phys. Rev. D* **59**, 024007 (1999), [arXiv:gr-qc/9810065 \[gr-qc\]](#).
- [85] I. Hinder *et al.*, *Class. Quant. Grav.* **31**, 025012 (2014), [arXiv:1307.5307 \[gr-qc\]](#).
- [86] Z. B. Etienne, Y. T. Liu, and S. L. Shapiro, *Phys. Rev. D* **82**, 084031 (2010).
- [87] M. D. Duez, Y. T. Liu, S. L. Shapiro, and B. C. Stephens, *Phys. Rev. D* **69**, 104030 (2004), [arXiv:astro-ph/0402502 \[astro-ph\]](#).
- [88] Z. B. Etienne, V. Paschalidis, Y. T. Liu, and S. L. Shapiro, *Phys. Rev. D* **85**, 024013 (2012).
- [89] B. D. Farris, R. Gold, V. Paschalidis, Z. B. Etienne, and S. L. Shapiro, *Phys. Rev. Lett.* **109**, 221102 (2012).
- [90] M. D. Duez, P. Marronetti, S. L. Shapiro, and T. W. Baumgarte, *Phys. Rev. D* **67**, 024004 (2003).
- [91] K. Taniguchi, T. W. Baumgarte, J. A. Faber, and S. L. Shapiro, *Phys. Rev. D* **77**, 044003 (2008).
- [92] D. Christodoulou, *Phys. Rev. Lett.* **25**, 1596 (1970).
- [93] M. Ruiz, V. Paschalidis, and S. L. Shapiro, *Phys. Rev. D* **89**, 084045 (2014), [arXiv:1402.5412 \[astro-ph.HE\]](#).
- [94] A. Tsokaros, M. Ruiz, V. Paschalidis, S. L. Shapiro, and K. Uryū, *Phys. Rev. D* **100**, 024061 (2019), [arXiv:1906.00011 \[gr-qc\]](#).
- [95] A. Tsokaros, K. Uryu, M. Ruiz, and S. L. Shapiro, *Phys. Rev. D* **98**, 124019 (2018), [arXiv:1809.08237 \[gr-qc\]](#).
- [96] G. B. Cook, S. L. Shapiro, and S. A. Teukolsky, *Astrophys. J.* **398**, 203 (1992).
- [97] G. B. Cook, S. L. Shapiro, and S. A. Teukolsky, *Astrophys. J.* **422**, 227 (1994).
- [98] G. B. Cook, S. L. Shapiro, and S. A. Teukolsky, *Astrophys. J.* **424**, 823 (1994).
- [99] M. Shibata, T. Baumgarte, and S. Shapiro, *Astrophys. J.* **542**, 453 (2000), [astro-ph/0005378](#).
- [100] V. Paschalidis and N. Stergioulas, *Living Rev. Rel.* **20**, 7 (2017), [arXiv:1612.03050 \[astro-ph.HE\]](#).
- [101] K. C. B. New and S. L. Shapiro, *Astrophys. J.* **548**, 439 (2001), [arXiv:astro-ph/0010172 \[astro-ph\]](#).
- [102] B. D. Farris, Y. T. Liu, and S. L. Shapiro, *Phys. Rev. D* **81**, 084008 (2010).
- [103] V. Paschalidis, Z. B. Etienne, and S. L. Shapiro, *Phys. Rev. D* **88**, 021504 (2013).
- [104] K. Kiuchi, Y. Sekiguchi, K. Kyutoku, M. Shibata, K. Taniguchi, and T. Wada, *Phys. Rev. D* **92**, 064034 (2015), [arXiv:1506.06811 \[astro-ph.HE\]](#).
- [105] Z. B. Etienne, Y. T. Liu, S. L. Shapiro, and T. W. Baumgarte, *Phys. Rev. D* **79**, 044024 (2009), [arXiv:0812.2245 \[astro-ph\]](#).
- [106] E. Barausse and A. Buonanno, *Phys. Rev. D* **81**, 084024 (2010), [arXiv:0912.3517 \[gr-qc\]](#).
- [107] M. Ruiz, A. Tsokaros, V. Paschalidis, and S. L. Shapiro, *Phys. Rev. D* **99**, 084032 (2019), [arXiv:1902.08636 \[astro-ph.HE\]](#).
- [108] R. Gold, V. Paschalidis, Z. B. Etienne, S. L. Shapiro, and H. P. Pfeiffer, *Phys. Rev. D* **89**, 064060 (2014), [arXiv:1312.0600 \[astro-ph.HE\]](#).
- [109] R. F. Penna, J. C. McKinney, R. Narayan, A. Tchekhovskoy, R. Shafee, and J. E. McClintock, *MNRAS* **408**, 752 (2010).
- [110] J. H. Krolik and J. F. Hawley, in *The Multicolored Landscape of Compact Objects and Their Explosive Origins*, American Institute of Physics Conference Series, Vol. 924, edited by T. di Salvo, G. L. Israel, L. Piersant, L. Burderi, G. Matt, A. Tornambe, and M. T. Menna (2007) pp. 801–808, [astro-ph/0611605](#).
- [111] E. Berger, *Ann. Rev. Astron. Astroph.* **52**, 43 (2014).
- [112] N. Vlahakis and A. Königl, “Relativistic Magnetohydrodynamics with Application to Gamma-Ray Burst Outflows. I. Theory and Semianalytic Trans-Alfvénic Solutions,” (2003).
- [113] Y.-C. Zou and T. Piran, *Monthly Notices of the Royal Astronomical Society* **402**, 1854 (2010), <https://academic.oup.com/mnras/article-pdf/402/3/1854/3126764/mnras0402-1854.pdf>.
- [114] K. S. Thorne, R. H. Price, and D. A. Macdonald, *The Membrane Paradigm* (Yale University Press, New Haven, 1986).
- [115] I. Shivers and E. Berger, *Astrophys. J.* **734**, 58 (2011), [arXiv:1101.0603 \[astro-ph.HE\]](#).
- [116] S. S. Komissarov, *Mon. Not. Roy. Astron. Soc.* **326**, L41 (2001).
- [117] K. Hayashi, K. Kawaguchi, K. Kiuchi, K. Kyutoku, and M. Shibata, (2020), [arXiv:2010.02563 \[astro-ph.HE\]](#).
- [118] B. D. Metzger, *Living Rev. Rel.* **20**, 3 (2017), [arXiv:1610.09381 \[astro-ph.HE\]](#).
- [119] L.-X. Li and B. Paczynski, *Astrophys. J. Lett.* **507**, L59 (1998), [arXiv:astro-ph/9807272](#).
- [120] J. Barnes and D. Kasen, *Astrophys. J.* **775**, 18 (2013), [arXiv:1303.5787 \[astro-ph.HE\]](#).
- [121] B. P. Abbott *et al.* (VIRGO, LIGO Scientific), (2013), [10.1007/lrr-2016-1](#), *Living Rev. Rel.* **19**, 1 (2016).
- [122] M. Campanelli, C. O. Lousto, and Y. Zlochower, *Phys. Rev. D* **74**, 041501 (2006).
- [123] P. Tsatsin and P. Marronetti, *Phys. Rev. D* **88**, 064060 (2013).
- [124] W. Kastaun, F. Galeazzi, D. Alic, L. Rezzolla, and J. A. Font, *Phys. Rev. D* **88**, 021501 (2013), [arXiv:1301.7348 \[gr-qc\]](#).
- [125] T. Dietrich, S. Bernuzzi, M. Ujevic, and W. Tichy, *Phys. Rev. D* **95**, 044045 (2017), [arXiv:1611.07367 \[gr-qc\]](#).
- [126] W. E. East, V. Paschalidis, F. Pretorius, and A. Tsokaros, *Phys. Rev. D* **100**, 124042 (2019), [arXiv:1906.05288 \[astro-ph.HE\]](#).
- [127] D. Shoemaker, LIGO Report No. LIGO-T0900288-v2, 2009, the high-power detuned model used in this paper is given in the data file ZERO_DET_HIGH.Pxf.TXT.
- [128] M. Ruiz, R. Takahashi, M. Alcubierre, and D. Nunez, *Gen. Rel. Grav.* **40**, 2467 (2008).
- [129] P. Ajith, M. Boyle, D. A. Brown, S. Fairhurst, M. Hannam, I. Hinder, S. Husa, B. Krishnan, R. A. Mercer, F. Ohme, C. D. Ott, J. S. Read, L. Santamaria, and J. T. Whelan, [arXiv e-](#)

- prints (2007), [arXiv:0709.0093 \[gr-qc\]](#).
- [130] J. Nelder and R. Mead, *Comput. J.* **7**, 308 (1965).
 - [131] B. Allen, W. G. Anderson, P. R. Brady, D. A. Brown, and J. D. E. Creighton, *Phys. Rev. D* **85**, 122006 (2012).
 - [132] I. Harry and T. Hinderer, *Classical and Quantum Gravity* **35**, 145010 (2018).
 - [133] E. Baird, S. Fairhurst, M. Hannam, and P. Murphy, *Phys. Rev. D* **87**, 024035 (2013), [arXiv:1211.0546 \[gr-qc\]](#).
 - [134] K. Belczynski, M. Dominik, T. Bulik, R. O’Shaughnessy, C. Fryer, and D. E. Holz, *Astrophys. J. Letters* **715**, L138 (2010).